UNIVERSITÀ DEGLI STUDI DI BARI
Dipartimento Interateneo di Fisica M. Merlin

DOTTORATO DI RICERCA IN FISICA
Ciclo XXXII
Activities report of the III years

The CMS RPC system upgrade project for HL-LHC

Supervisore:
Ch.ma Prof.ssa Gabriella Pugliese

Dottorando:
Dott. Andrea Gelmi

Coordinatore:
Ch.mo Prof. Giuseppe Iaselli

My PhD research activity concerned the upgrade project for the CMS Resistive Plate Chambers (RPC) system in view of the High Luminosity-LHC (HL-LHC) period [1–3]. The research work has been mainly focused on the four following topics:

- aging studies of the RPC system during LHC and for the future HL-LHC;
- RPC system extension at the high eta region;
- search for RPC eco-friendly gas mixture;
- L1 Muon trigger study.

1 Aging studies on CMS RPC

1.1 Aging studies of the CMS RPC system during LHC

The CMS RPC system was designed to provide muon identification, excellent triggering, timing and momentum measurements at the nominal LHC luminosity of $10^{34}\ cm^{-2}s^{-1}$, for 10 years of operation [1, 4]. After almost seven years of operation, the CMS RPC system shows stable performance and high efficiency [5]. The RPC hit efficiency and the muon cluster size histories during LHC Run II period are reported in Figure 1, for barrel and endcap.

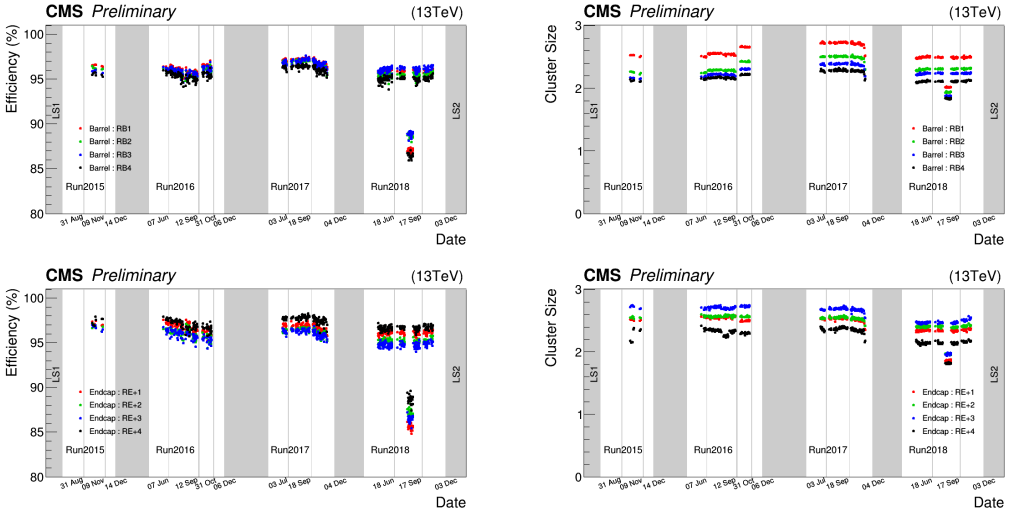

Figure 1: CMS RPC efficiency (left) and muon cluster size (right) monitored during Run II as a function of time. The plots on top represent the barrel stations, while on bottom the positive Endcap stations. Results for the negative disks are similar.

Nevertheless, a general ohmic currents increase was observed during 2018, when the LHC instantaneous luminosity increased, reaching almost twice the nominal value.

Figure 2 (left) shows the average ohmic currents, measured at 6.5 kV, in four representative RPC stations: W0 in the barrel and RE+1, RE+4, RE-4 in the endcap. The ohmic currents increase is directly correlated with the background rate distribution, indeed, the increase is more evident in the external detector stations such as RE+4 and RE-4, where the background rate is $\approx 40\ Hz/cm^2$; while the ohmic currents are almost stable with a minimal increase in the inner detector stations such as W0 and RE+1, where the background rate is less than 10 Hz/cm^2.

As shown in Figure 2 (left), the ohmic currents were observed to decrease during the periods with no collisions, such as the Technical Stops (TS), or during the periods with very low instantaneous luminosity, such as the Heavy Ions (HI) collision periods. The observed ohmic currents increase seems therefore to be not a permanent effect, but rather the measurements show at least a partially recoverable effect.

Another parameter which plays an important role for the ohmic current stability is the gas flow. The exchange of the gas volume allows removing the pollutants created by the radiation in

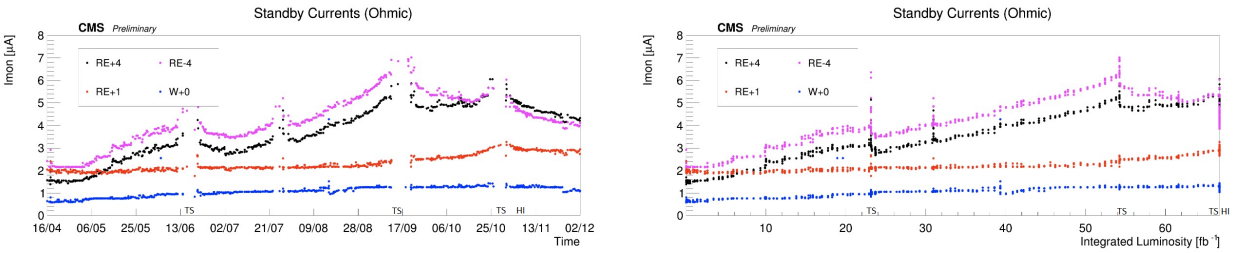

Figure 2: Ohmic currents measured as a function of time (left) and as a function of the integrated luminosity (right). The currents were measured during 2018 in four RPC stations: W0 in the barrel and RE+1, RE+4, RE-4 in the endcap.

the detector gas gap, preventing the deposition on the inner surface and thus ensuring its integrity. The RE-4 and RE+4 stations operate in similar conditions in terms of background rate and gas flow. After the TS2, around the middle of September, the gas flow has been doubled in RE-4 station, from one to two gas volume exchanges per hour, and a significant change in its ohmic current behaviour has been observed. The increase of the gas flow allowed to mitigate the ohmic currents increase, which is instead visible in the RE+4 station. The higher gas flow in RE-4 also allowed a faster ohmic current recovery during the heavy ion collisions period, up to the point that it drops below the RE+4 curve.

Figure 2 (right) shows a roughly linear dependence of the ohmic current as a function of the integrated luminosity. The slopes of W0 and RE+1 stations are similar since the operating conditions are similar, and the same is true for RE+4 and RE-4 stations.

In conclusion, the background rate and the gas flow are the two main parameters that influence the ohmic current, and

1.2 Hydrogen Fluoride (HF) study

The CMS RPC gas mixture is based on HydroFluorocarbon components, in particular it is composed by: 95.2% $C_2H_2F_4$, 4.5% iC_4H_{10} and 0.3% SF_6 [1]. The decomposition of the $C_2H_2F_4$ molecules, induced by the relatively high-energy photons generated during the charge multiplication, produces a significant concentration of fluorine ions (F^-). The fluorine ions can combine with Hydrogen (H^+) to produce Hydrogen Fluoride (HF) acid [6]. If the HF is not efficiently removed by the gas flow and it remains for a not negligible time inside the gas gap, it may represents a possible cause of the detector inner surface damaging due to its high chemical reactivity. Additionally, the HF may form a thin conductive layer on the inner gap surface, decreasing the surface resistivity. The effects induced by the HF may lead to an increase of the dark current and the noise counting rate, which could affect the detector performance.

1.2.1 HF study at GIF++

The HF production mechanism has been studied in detail at the CERN Gamma Irradiation Facility (GIF++) to better understand and to estimate the influence of the background rate and the gas flow [7, 8].

The measurement technique is based on specific ion-selective electrode (ISE) [6]. During the measurements, the exhaust gas from an irradiated spare CMS RPC endcap chamber flows in a TISAB (Total Ionic Strength Adjustment Buffer) and distilled water solution (50-50%), where the ISE allows the F^- measurements.

The measurements have been performed at different background rate conditions, and operating the detector with three different gas flows: 0.2, 1 and 3 gas volume exchanges per hour. The results are reported in Figure 3 (left). The plot shows a linear dependence of the HF production rate on the background rate (and relative background current). The HF slope depends instead on the gas flow, higher is the gas flow and less is the HF concentration. These results prove the HF dependence on the background rate and on the gas flow.

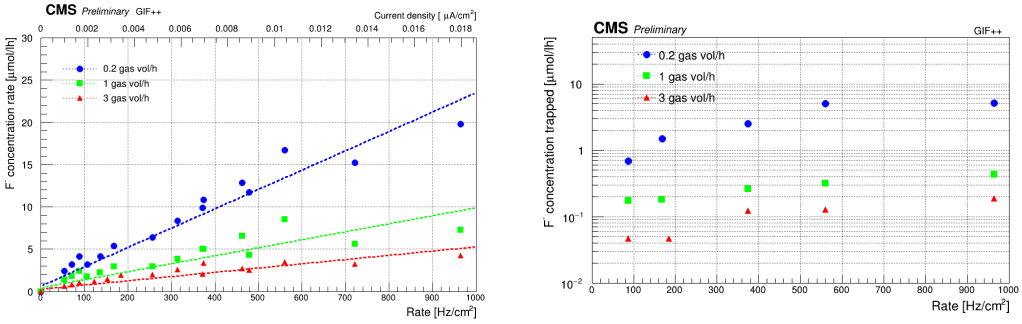

Figure 3: Left: fluoride concentration rate as a function of the background rate, measured with three different gas flow: 0.2, 1 and 3 gas volume exchanges per hour. Right: F^- concentration trapped inside the gas gap and not efficiently removed. The concentration was measured at different background rate, and with three different gas flow. The estimation was done considering the F^- accumulated during 8 hours of measurements, just after the detector switch off.

Finally, Figure 3 (right) shows the concentration of HF not efficiently removed by the gas flow and thus trapped inside the gas gap. The estimation was done considering the HF accumulated during the 8 hours just after switching off the detector. The results show that the concentration of the HF trapped inside the gas gap increases at high background rate, when the HF production is high. Above all, the concentration of the HF trapped depends on the gas flow: higher is the gas flow and less is the HF trapped.

The probability that HF deposits on top of the inner gap surface, with consequent damage, obviously increase with the HF concentration and with the increase of time that remains inside the gas gap.

The HF measured at the exhaust gas represents the quantity extracted, more or less efficiently, from the gas gap by the gas flow. If the HF is a cause of detector aging, then a fraction of the HF produced must be absorbed by the inner gap surfaces. To check the HF absorption hypothesis, the detector was turned off for 20 days, after which it was operated with argon. A residual HF signal was still measured, but since neither $C_2H_2F_4$ nor SF_6, but only argon was used, the HF could not be produced but could only be extracted from the gap surface. The current circulating in the argon forced the further extraction of the HF, which was bound to the inner detector surface.

In conclusion, the HF measurements at GIF++ demonstrate that the HF production rate depends on the background rate and the concentration depends on the gas flow. It has also been proved that the HF can be trapped and deposit inside the gas gap if the gas flow is not enough with respect to the HF production rate, and it is possible to remove it (or partially remove it) operating the detector with argon.

1.2.2 HF study in CMS

The HF measurements have been performed in CMS during Run II, in order to study the possible detector aging and to investigate the observed ohmic current increase [8]. The HF measurement method was the same as used at GIF++, and performed at the exhaust gas of three stations:

- Endcap RE+4, which operates with 1 gas volume exchange per hour, and where the background rate is $\approx 40\ Hz/cm^2$;
- Endcap RE+1, which operates with 0.6 gas volume exchanges per hour, and where the background rate is less than 10 Hz/cm^2;
- Barrel W0, which operates with 0.6 gas volume exchanges per hour, and where the background rate is less than 10 Hz/cm^2.

The fraction of exhaust gas flowing in the solution was kept constant at 0.5 l/h. The accumulated HF concentrations were periodically measured and are reported in Figure 4 (left) as a function of

time. All the three curves follow the same trend in time, driven by the LHC operation. Stations RE+1 and W0 accumulated a similar amount of HF, indeed the operating conditions in terms of gas flow and background are similar. In RE+4 station the amount of HF accumulated is around 2.5 times higher than W0 and RE+1 stations, but in this case the background rate is around 4 times higher, and the gas flow around two times greater.

The HF concentration follows a linear trend with respect to the integrated luminosity, shown in Figure 4 (right), in a similar way as it was observed for the ohmic current in Figure 2 (right). In agreement with the ohmic current analysis, the HF slope of RE+4 station is greater than the slopes of W0 and RE+1 stations, which are similar since the operating conditions. The results are in agreement with the GIF++ measurements, proving the HF dependence on the background rate and the gas flow.

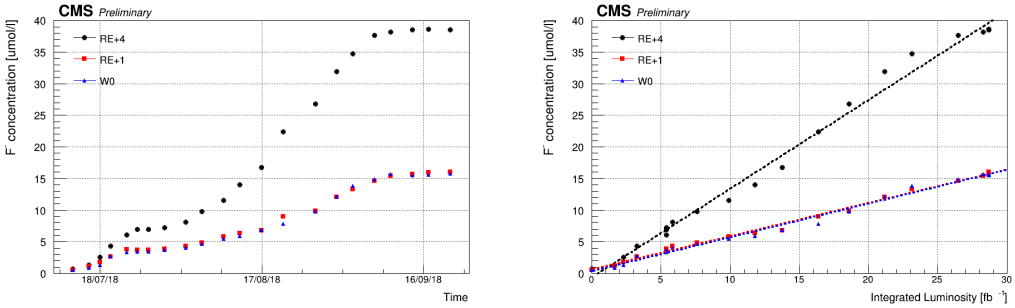

Figure 4: F^- concentration as a function of time (left) and as a function of the integrated luminosity (right). The measurements have been performed during Run II (July - October 2018) at the gas exhaust of 3 stations: W0 in the barrel and RE+1, RE+4 in the endcap.

Finally, Figure 5 shows the linear dependence between the ohmic currents and the F^- concentration. The RE+1 and W0 slopes are similar and small, with a low background rate. Consequently, the HF production is low, and the current stability shows that the gas flow is enough to efficiently remove the HF produced. On the other hand, the RE+4 slope is larger, the background rate is higher, the HF production is consequently higher, and the results show that the gas flow is not sufficient to efficiently remove the HF produced. Hence the HF likely to be trapped inside the gas gap damaging the inner surface and creating a thin conductive layer causing the observed ohmic current increase.

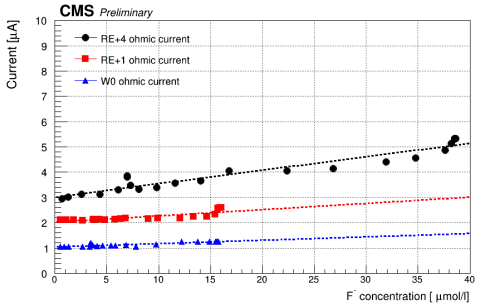

Figure 5: Ohmic current as a function of the F^- concentration.

From these results it is clear that the gas flow must be adjusted as a function of the background rate. A new parameter (G_r), that represents the gas volume exchanges per unit of background rate, is proposed to estimate the optimal gas flow to set as a function of the background. It was shown that W0 and RE+1 stations have almost stable ohmic current, therefore their G_r can be considered as an optimal value to use and to keep constant. For W0 and RE+1 it results $G_r = 0.06 \frac{vol/h}{Hz/cm^2}$, while for RE+4 $G_r = 0.025 \frac{vol/h}{Hz/cm^2}$. The G_r values of RE+4 is $\approx$ 2.5 times smaller than W0

and RE+1, therefore the RE+4 gas should be increased by a factor ≈ 2.5. In agreement with the obtained results, e.g. Figure 2(left), when the RE+4 gas flow was doubled the ohmic current increase was mitigated, and it even inverted the trend.

The results are very important and have to be taken into account in view of the next LHC and HL-LHC runs, when the luminosity will increase. In conclusion, for good detector operations it is necessary to fine tune the gas flow as a function of the background rate so that the HF is efficiently removed.

1.3 Long-term aging studies on CMS RPC for HL-LHC

During Run I and Run II the CMS RPC system did not show any evident aging effects after collecting $\approx 10\ mC/cm^2$ of integrated charge [5]. Nevertheless, durin the High Luminosity LHC (HL-LHC) period, the instantaneous luminosity will reach $5 \times 10^{34}\ cm^{-2}s^{-1}$ (factor five more then the nominal LHC luminosity), providing to CMS an additional integrated luminosity of about 3000 fb^{-1} over 10 years of operation.

Run I and Run II data have been used to estimate the maximum background rate during HL-LHC, foreseen in $\approx 600\ Hz/cm^2$, and the equivalent maximum integrated charge collected at the end of the HL-LHC period estimated in 840 mC/cm^2. These estimations include a safety factor of 3 [3].

A new longevity test is then needed to estimate the impact of the HL-LHC conditions, in order to very if the RPC system will efficiently operate for the full period [9, 10]. Since 2016, I am in charge of the RPC longevity test ongoing at GIF++.

Four spare Endcap chambers (two RE2/2 and two RE4/2 chambers) have been installed at GIF++. In order to study the longevity of the detectors, two chambers out of four (one RE2/2 and one RE4/2), are continuously operated under gamma irradiation, while the remaining two chambers are turned on only time to time and used as reference. The chambers operate with the standard gas mixture and are irradiated at $\approx 600\ Hz/cm^2$ at the working point voltage ($\approx 9.8\ kV$). At present, about 600 mC/cm^2 and 328 mC/cm^2 have been integrated for RE2/2 and RE4/2 irradiated detectors, which correspond approximately to 71% and 39% of the expected HL-LHC integrated charge.

The main detector parameters are monitored and periodically compared with those of the reference chambers. Moreover, when the muon beam is available, the detector performance is studied at different background rate. The results are reported below.

1.3.1 Detectors perameter monitoring

In order to spot possible degradations of inner gap surface induced by the radiation, the detector noise rate and dark current are periodically measured when the GIF++ source is off, for both irradiated and non-irradiated reference chambers.

Figure 6 (left) shows the RE2/2 dark currents curves measured at different integrated charge values. The dark current is almost stable in time, a part negligible small variations that follow the environmental temperature and humidity. No significant dark current variations have been observed so far, and the values remain low as measured during the chamber production certification.

Figure 6 (right) shows the average noise rate at 9.6 kV, monitored as a function of the integrated charge for both the RE2/2 irradiated and reference chambers. The noise rate is almost stable in time and lower than 1 Hz/cm^2.

The low and stable dark current and noise rate indicate a good state and quality of the inner gaps surface, excluding any possible aging damaging so far.

1.3.2 Detectors performance monitoring

During the Test Beam (TB) periods at GIF++, the detectors performance is tested with a muon beam in presence of different background conditions.

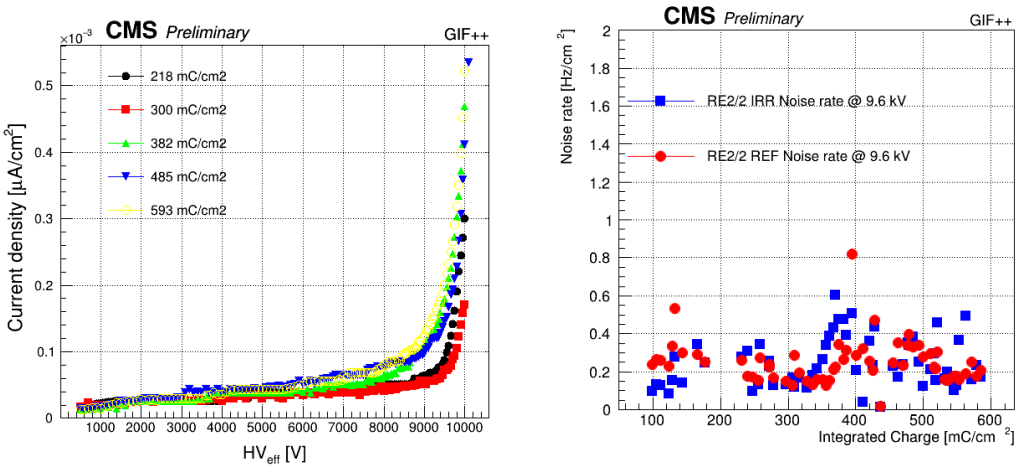

Figure 6: Left: RE2/2 irradiated chamber currents curves at different integrated charge values. Right: average noise rate versus the integrated charge, for RE2/2 irradiated (blues) and reference (red) chamber, at 9.6 kV.

Figure 7 (left) represents the RE2/2 irradiated chamber efficiency curves as a function of the HV_{gas}, measured at different background radiation (up to $\approx$ 600 Hz/cm^2) and at different integrated charge. The use of HV_{gas} in place of HV allows describing the system independently from the voltage drop across the electrodes due to the background current and HPL resistance [11]. All the efficiency curves overlap proving that the performance is stable in time.

The detectors performance has been measured at different background radiation conditions. Figure 7 (right) shows the RE2/2 irradiated chamber efficiency at the working point as a function of the background rate, measured at different accumulated charge. The efficiency is stable in time, with a 2% decrease at the highest expected background rate, 600 Hz/cm^2. This result proves the detectors efficiency stability, and overall that the detectors are able to work efficiently at the maximum expected rate during HL-LHC.

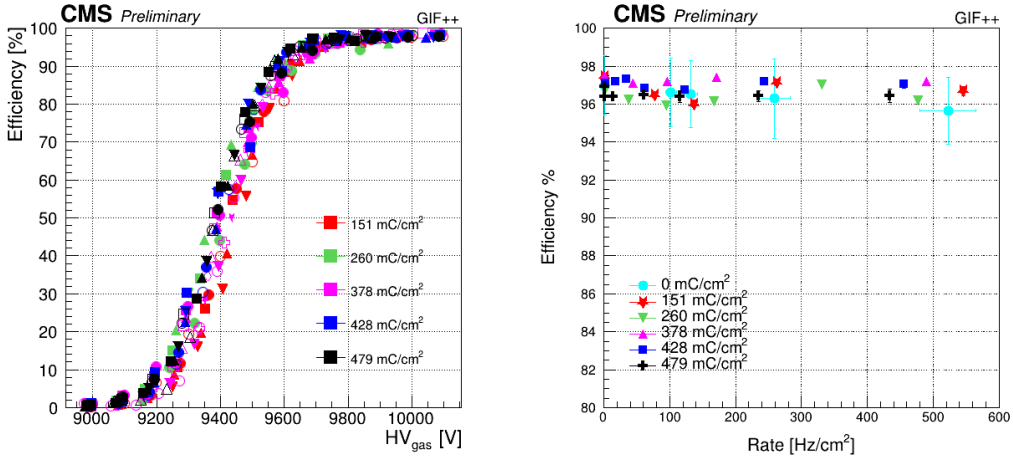

Figure 7: Left: RE2/2 irradiated chamber efficiency as a function of the HV gas, at different background irradiations and at different integrated charge values. Right: RE2/2 irradiated chamber efficiency at working point as a function of the background rate, measured at different integrated charge values.

In conclusion, all the results of the longevity test at GIF++ show stable detectors parameters and performance, after having collected a significant amount of integrated charge, $\approx$ 600 mC/cm^2, which correspond to $\approx$ 2.5 the expected integrated charge at HL-LH without considering the safety factor. Definitely, no evidence of aging effects have been observed so far.

2 RPC system extension at the high eta region

In view of the HL-LHC phase, the RPC system will extend the muon eta acceptance from $|\eta| = 1.8$ to 2.4 in order to complement the existing ME3-4/1 stations equipped with CSC only, increasing the muon system redundancy, and to extend the contribution of RPCs for both muon tracking and triggering in the forward region.

The two endcap stations RE3-4/1 will be equipped with a new generation of improved RPC (iRPC) [12]. The extensive R&D activity allowed to define the baseline for the new iRPC detectors, which are based on the RPC technology, but having higher rate capability that allows to efficiently operate at the high eta region. The higher rate capability was achieved using lower electrodes resistivity, $0.9 \div 3 \times 10^{10} \Omega cm$, and thinner electrodes and gas gap thickness, equal to 1.4 mm with respect to the 2 mm of the standard RPCs. These modifications allow shortening the recovery time of the electrodes and reducing the total charge produced in a discharge. The resulting loss in gas gain is compensated by the lower threshold and higher signal amplification of the new front-end electronics board (FEB). The FEB uses the ASIC PETIROC based on SiGe technology, it includes a fast preamplifier with a gain of 25 [13]. The ASIC also includes a Time Digital Converter (TDC) to measure the signal arrival time. The strips are read out from both ends, and the arrival time difference of the two signals is used to determine the particle position along the strip (η position).

2.1 Background rate study for the iRPC at HL-LHC

The estimation of the expected radiation level during HL-LHC is important to determine the detector performance and longevity. For these reasons, the background rate expected during HL-LHC in the RE3-4/1 stations was studied in detail.

The expected incident fluxes (ϕ_{bkg}) were estimated by implementing the upgraded CMS geometry for HL-LHC in the FLUKA simulation (CMS Fluka study version v.3.7.7.0) [3]. The estimation of the background rate ($r(E)$) was done scaling the simulated incident background fluxes with the detector sensitivity ($S(E)$).

$$r(E) = \phi_{bkg} \times S(E) \tag{1}$$

The sensitivity represents the detector response to the background particles, and is defined as the probability for an incident particle at a given energy, reaching the detector surface, to produce a signal:

$$S(E) = \frac{r(E)}{\phi_{bkg}}(E) \tag{2}$$

The sensitivity is dependent on the detector geometry, and it is a function of the type of the incoming particles and their energy, indeed for different particles with different energies, different processes are responsible for the production of secondary particles.

In order to study the detector sensitivity, the iRPC geometry has been described and simulated using the GEANT tookit, based on Monte Carlo methods.

First of all, the iRPC sensitivity has been studied with respect to the gamma background at GIF++, comparing the simulation and the experimental results in order to validate the simulated geometry.

Figure 8 (left) shows the detector cluster rate at working point experimentally measured (red curve) at GIF++ at different background conditions (ABS), compared with the simulated rate (black curve). A factor ≈ 2 difference between the two curves is observed. To better match the experimental data and the simulated data, an energy threshold of 100 keV was applied to the simulated primary and secondary charged particles which produce the signal in the gas gaps, in order to simulate the electronics threshold used for the experimental measurements (300 $\mu V \approx 50\ fC$).

Likewise, Figure 8 (right) shows the detector gamma sensitivity comparison between experimental data and simulated data, including the curves with the applied charged particles energy thresholds. The good agreement between simulated and experimental results allowed to validated

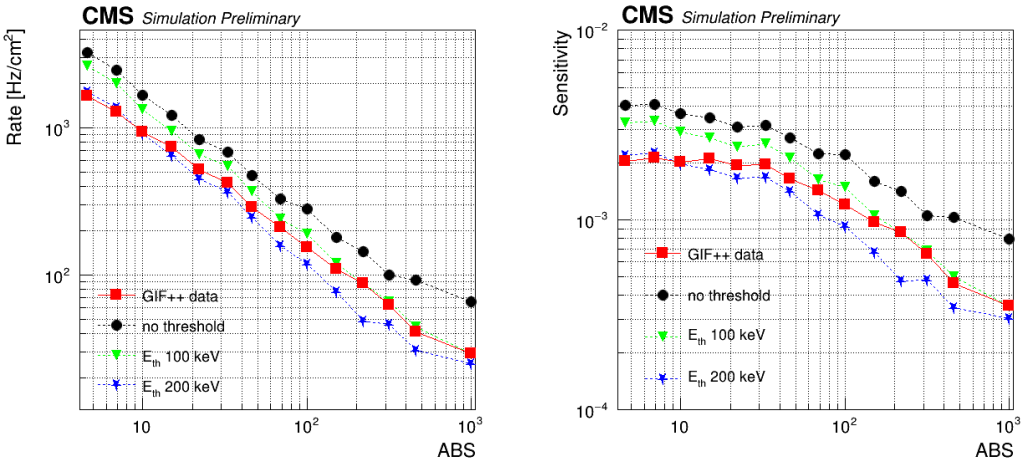

Figure 8: Rate (right) and sensitivity (left), measurements at different background conditions (ABS). The plots show the comparison between experimental data from GIF++ (red squares) and simulated data: without charged particles energy threshold (black) and with charged particles energy thresholds of 100 keV (green) and 200 keV (blue).

the simulated iRPC geometry, and use it for the iRPC background rate estimation at HL-LHC.

The detector sensitivity was studied with respect to the different particles that compose the CMS background at the expected HL-LHC spectra: neutrons, photons and charged particles. The results are shown in Figure 9 (left), where the iRPC sensitivity is reported as a function of the energy of the incoming particles.

The gamma sensitivity values rise at the high energy region, indeed, at low gammas energy the produced secondary charged particles have not enough energy to reach the gas volume. The contribution from different processes to the gamma sensitivity has been studied and the result is reported in Figure 9 (right). As expected the dominant contribution is due to the Compton effect up to energies of few MeV, while at higher energies (greater than $10MeV$) the dominant process is the pair production. Photoelectric contribution is relevant only at very low energies.

The neutron sensitivity values rise at the low energy region ($E_n < 10^{-5}$ MeV), which is mostly due to gammas coming from the (n, γ) capture reaction, whose cross section increases with decreasing in neutron energy as $\sigma \propto 1/\sqrt{E_n}$. At higher energies ($E_n > 1$ MeV), the neutron sensitivity rises rapidly as a consequence of protons produced by elastic scattering on Hydrogen and by (n, p) reactions with Carbon, Oxygen and Aluminium. Finally, Figure 10 (left) shows the expected background rate in RE3/1 station as a function of the incident particles energy, estimated from the convolution of the sensitivities and the incident particles fluxes, using Formula 2.

The average background rate has been estimated using the average sensitivity values, [n (0.4%), γ (2.4%), $e^{-/+}$ (6.8%)]. Figure 10 (right) shows the contribution of the different particles to the total background rate in the RE3/1 station as a function of the distance from the centre of the CMS beam pipe. The average background rate of ≈ 600 Hz/cm^2 defines the requirement of a minimum rate capability of ≈ 1.8 kHz/cm^2 for the iRPCs, when considering a safety factor of three. The same estimation has been done for the RE4/1 station as well, where the particles flux is a slightly lower, and the estimated background rate is ≈ 1.5 kHz/cm^2.

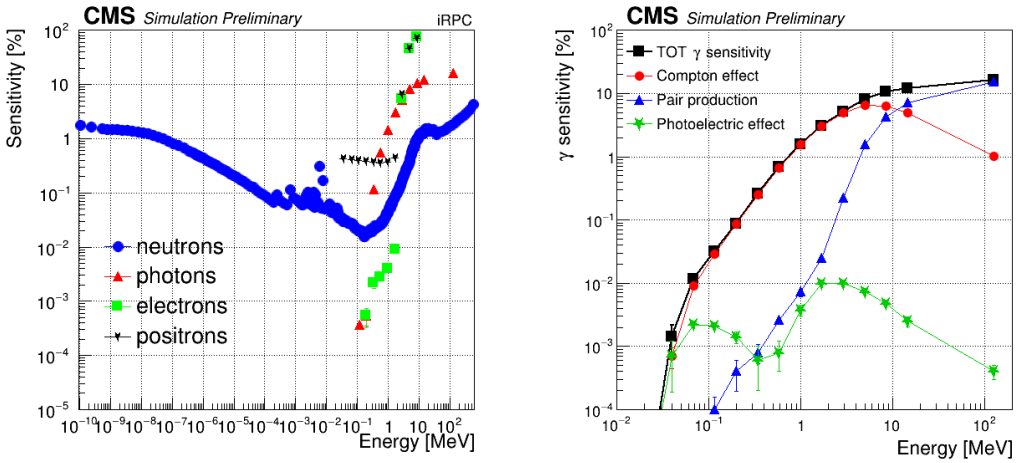

Figure 9: Left: Monte Carlo estimation of the iRPC sensitivity with respect to the different background particles (neutrons, photons, electrons and positrons) as a function of the kinetic energy of the incident particles. Right: contribution from the different processes to the detector gamma sensitivity (black) as a function of the gammas kinetic energy: Compton (red), pair production (blue) and photoelectric (green).

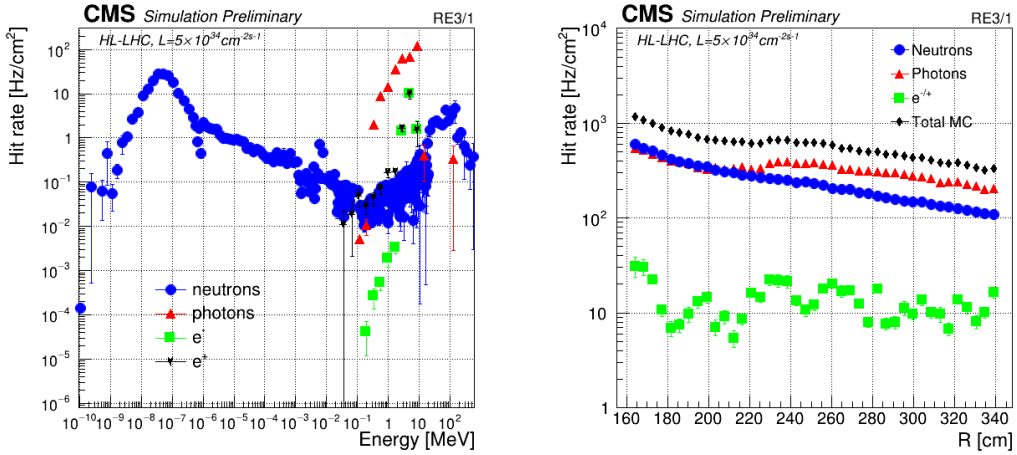

Figure 10: Monte Carlo simulation of the background rate expected in the endcap RE3/1 station during HL-LHC, as a function of the incoming particles energy (left) and as a function of the distance (R) from the centre of the CMS beam pipe (right). The contribution of the different particles is reported.

2.2 iRPC performance at GIF++

The new iRPC chambers are conceived such that the average avalanche charge associated to the passage of particles is reduced with respect to the standard CMS RPCs, in order to increase the rate capability and the detector longevity. Figure 11 shows the average charge measured at working point for standard RPC (black) $\approx$ 27 pC, and for the iRPC (red) $\approx$ 9 pC. The lowered FEB threshold and the narrow gas gap thickness of the iRPC, allowed to obtain an average charge $\approx$ 3 times smaller with respect to the standard RPC.

Extensive test of a large size iRPC equipped with the new FEB, performed at GIF++ with a muon beam, allowed to validate the iRPC performance under different background conditions. Figure 12 (left) represents the efficiency as a function of the effective high voltage measured at different particle rate. The results show that efficiencies higher than 95% are reached at the expected HL-LHC background rate of 1.8 kHz/cm^2. Figure 12 (right) shows the evolution of the efficiency at working point as a function of the background cluster rate. The muon efficiency was

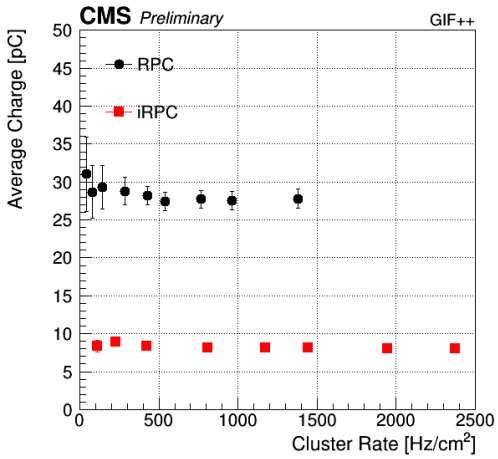

Figure 11: Average avalanche charge at working point as a function of the cluster rate, measured for the standard RPC (black) and iRPC (red).

calculated as:

$$\epsilon = \frac{\frac{N}{N_{trg}} - \frac{N_{bkg}}{N_{trg}}}{1 - \frac{N_{bkg}}{N_{trg}}} \tag{3}$$

Where ϵ is the measured muon efficiency, N is the number of muon events detected by the chamber from both ends of the strips, N_{trg} is the number of the muon triggers, and N_{bkg} is the number of the gamma background hits expected in the time interval.

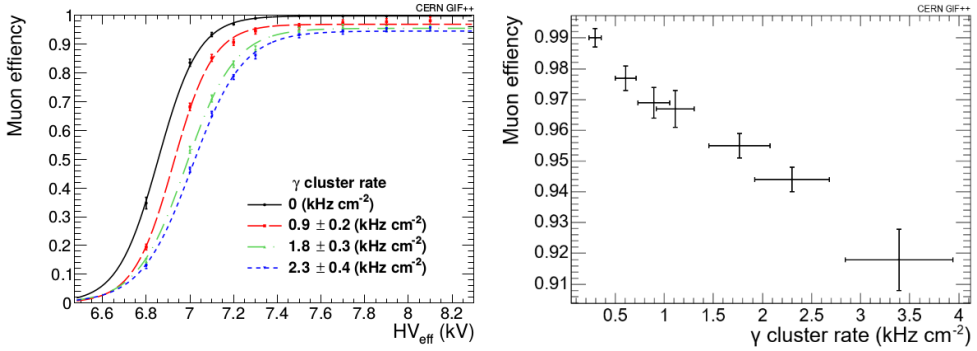

Figure 12: Left: efficiencies as a function of the effective high voltage measured at different background rate. Right: evolution of the efficiency at working point at different background cluster rate. The measurements were performed with 81 fC threshold.

The hits position along the strips were determined by using the time information from both ends of the strip, according to the Formula 4:

$$Y = L/2 - v\ (T_{HR} - T_{LR})/2 \tag{4}$$

Here T_{HR} and T_{LR} are the arrival times from the strip ends, v is the signal propagation velocity and L is the total strip length. A time resolution of 177 ps was measured, allowing the determination of the position along the strips with a spatial resolution of ≈ 1.7 cm.

Finally, the detector absolute time resolution was estimated in 368 ps.

2.3 iRPC longevity studies

Possible aging effects of the iRPC system must be taken into account and the detector longevity has to be validated for the entire HL-LHC program. The iRPC have to be validated up to $\approx 1\ C/cm^2$, which is the estimated integrated charge equivalent to the HL-LHC period.

The iRPC longevity test campaign is performed at GIF++, where a large size chamber (iRPC prototype-1) has been tested up to $\approx 90\ mC/cm^2$, and a second chamber (iRPC prototype-2) is still under irradiation, and currently has accumulated $\approx 100\ mC/cm^2$.

Figure 13 (left) shows the iRPC prototype-1 dark current and noise rate measured at 7 kV at different integrated charge values. From the results is evident the dark current increase, observed already just after the beginning of the irradiation. The dark current constantly increased, up to reach values of 70 μA. The detector performance has been tested and compared with that measured before the irradiation test. The dark current effects caused a significant decrease of the rate capability, as reported in Figure 13 (right).

Due to the impossibility to run the detector with a so high dark current and unstable conditions, it was decided to stop the irradiation test and to open the gas gaps to investigate the problem. The results of the inner gap surface analysis are reported below.

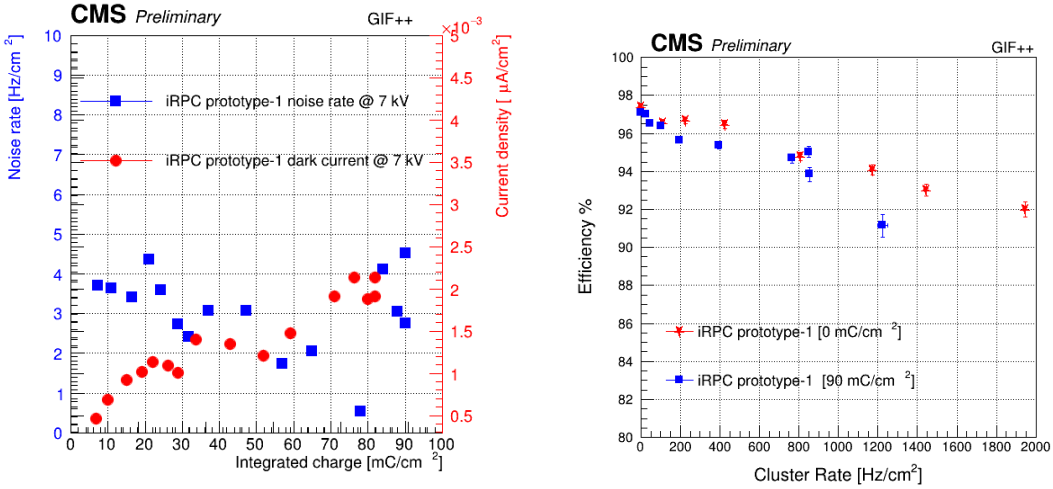

Figure 13: Left: iRPC prototype-1 dark currents (red) and noise rate (blue) monitoring versus integrated charge, at 7 kV (left). Right: iRPC prototype-1 efficiency at working point as a function of the gamma background cluster rate.

2.3.1 iRPC HPL surface analysis

The irradiation of the iRPC prototype-1 was forced to be stopped due to the impossibility to run the detector with a so high dark current and unstable conditions. In order to investigate the origin of the problem, the detector gaps have been opened and several analysis have been performed.

At the visual inspection the inner gaps surface presents sticky white matt spots nearby the spacers and the edges, as shown by Figure 14 (left). The spots seem to be drops of liquid, probably linseed oil not well polymerized, and they follow a preferential direction given by gravity. Both anode and cathode present the same configuration without any significant differences.

A not irradiated iRPC gap, produced in the same bunch, was opened and the inner surface shown the same structure as the irradiated one, with the only difference that the drops of liquid presented a brightness color instead to be white. Therefore, the surface defects are due to production problems, and the effect is made more visible by the irradiation.

A more accurate inspection was done using the Scanning Electron Microscope (SEM) technique. The SEM better shows the white matt spot nearby the spacer, which appears darker in Figure 14 (center) due to the surface variation effect. The SEM also underline a ring-shaped area, $\approx 5\ mm$ just around the spacer.

The inner gap surface profile was measured using the Vertical Scanning Interferometry (VSI) technique, and the result is reported in Figure 14 (right). The measurements represent the relative surface height with respect to an arbitrary reference point, chosen in the not-affected area. The surface profile highlight a lower height region around the spacers, and an higher height region

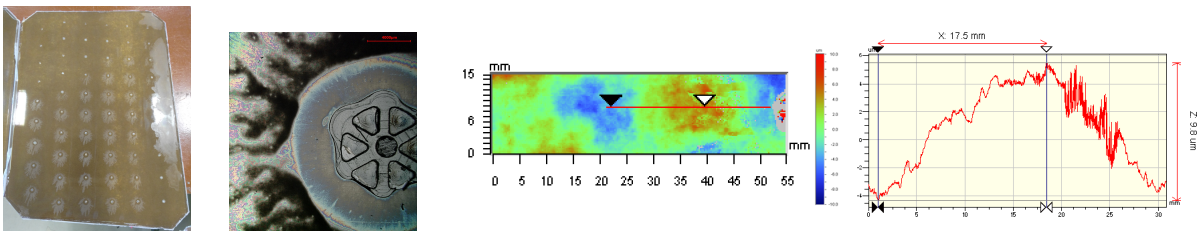

Figure 14: Left: pictures of the iRPC prototype-1 inner surface after the irradiation. Center: SEM image, of the iRPC prototype-1 area around a spacer. Right: VSI topography.

corresponding to the white matt area.

The chemical composition of the surface was studied using the Energy Dispersive X-ray Spectrometer (EDS/X-ray). The results excluded any chemical contaminations, but reported the significant presence of the Nitrogen in the ring-shaped area around the spacers, and the absence of the Nitrogen in the white matt area. The Nitrogen constitute the external HPL layers, therefore the results, in agreement with the other analysis, indicate a lack of oil in the ring-shaped area and a thicker oil layer in the white matt area.

The surface analysis have highlighted a production problem in the gaps oiling procedure, demonstrating the not uniform surface. The critical regions, where the oil layer is particularly inhomogeneous, have been identified: the area nearby the spacers and the edges present an accumulation of not polymerized linseed oil, while the ring-shaped area around the spacers presents a lack of oil.

The oiling procedure was the same adopted for the standard RPC, with just few differences: the HPL having lower roughness, and the new spacers having a slightly bigger and different bounding area geometry with respect to the 2005 RPC production.

The oiling procedure has been reproduced immersing HPL plates with the glued spacers inside the linseed oil, in order to be able to observe the dynamics of the oil distribution over the HPL plate and in particular near to the spacers and the edges. The problem was successfully reproduced, and what was observed is that the oil is pushed away from the spacers, probably due to their low surface tension and helped by the improved HPL roughness. The effect seems to be amplified by the new spacers geometry and by the capillary effect. The oil is pushed away from the spacers creating the ring-shaped areas having a very thin oil layer, while it is accumulated around 5 mm far from the pacers. Additionally, some linseed oil remains trapped in the new bigger bonding area and in the pockets created under the spacers lips. In that positions, the airflow flushing during the dry procedure to polymerize the oil is less, therefore the oil not fully polymerized slowly comes out creating drops traces on the surface.

In conclusion, the not-uniformity of the inner gaps surface are a production issue, and they are the cause of the observed dark current increase. In particular, the most critical problem is the not polymerized oil that can results in gas gap thickness variations and even electrical bridges between the HPL plates.

Test to fine tune the oil parameters and the oiling procedure are ongoing.

3 Search for RPC eco-friendly gas mixture

Recent European regulations demand the use of environmentally un-friendly gases, such as fluorinated gases, to be limited [15].

The Global Warming Potential (GWP) of the present CMS RPC gas mixture is around 1400, mainly given by the $C_2H_2F_4$, which is the main RPC gas component (95.2%).

The most promising candidates to replace the $C_2H_2F_4$ are the fluorinated propene refrigerants called hydro-fluoro-olefins (HFOs), which have a GWP less than 6, and they are already used in industrial applications [16]. The complete replacement $C_2H_2F_4$ with HFO as main gas component requires operation at much higher applied voltages, more than 13 kV. To overcome this problem, the addition of inert gas, such as 40% or 50% of CO_2, is necessary to reach acceptable working point values.

3.1 Eco-friendly gas mixture characterization under irradiation at GIF++

Very interesting results were produced in a previous R&D, testing with cosmic rays a 2 mm single-gap RPC, with 50% of $HFO-1234ze$, 45% of CO_2, 4.5% of iC_4H_{10} and 0.3% of SF_6 [3, 17].

Careful validation of the RPC performance in LHC-like conditions, using this ecogas mixtures, has to be carried out at GIF++ to study the rate capability and the detector aging. In this context, an R&D program has been set up among the CMS, ATLAS, ALICE Collaborations and CERN-EP-DT group [18]. The experimental set up at GIF++ consists of 5 chambers: 3 single-gap RPCs having 2 mm gas gap and plates thickness, from ATLAS, ALICE and EP-DT, 1 double gap CMS RPC and 1 double gap CMS improved-RPC .

The chambers have been tested at different gamma background conditions, and the currents measured with the ecogas mixture were compared with those measured with the standard mixture, as reported in Figure 15. At the same background rate conditions, the results show a ≈ 2 kV shift for the CMS RPC (left plot) when working with ecogas, and ≈ 1.2 kV for the CMS iRPC (right plot) when working with ecogas, in agreement with the results found in the previous R&D [3].

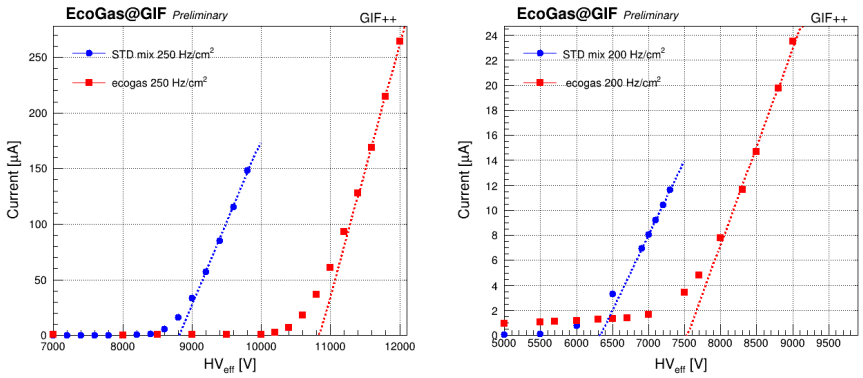

Figure 15: Currents versus the effective high voltage, measured in presence of gamma background with the standard gas mixture and with the ecogas mixture. Currents measurements performed for CMS RPC (left), and for CMS-iRPC (right).

The average avalanche charge in RPC operating with the ecogas mixture was studied, and as reported in Figure 16 (left), it was found to be ≈ 150 pC at the working point, around 5 times greater with respect to the standard mixture. The average gamma cluster size has been studied as well, and as shown in Figure 16 (right) it was measured ≈ 2.6 strips at the working point for the ecogas mixture, while ≈ 1.8 strips with the standard mixture.

Detailed test are planned at GIF++ to study the detector performance using the ecogas mixture under high background rate.

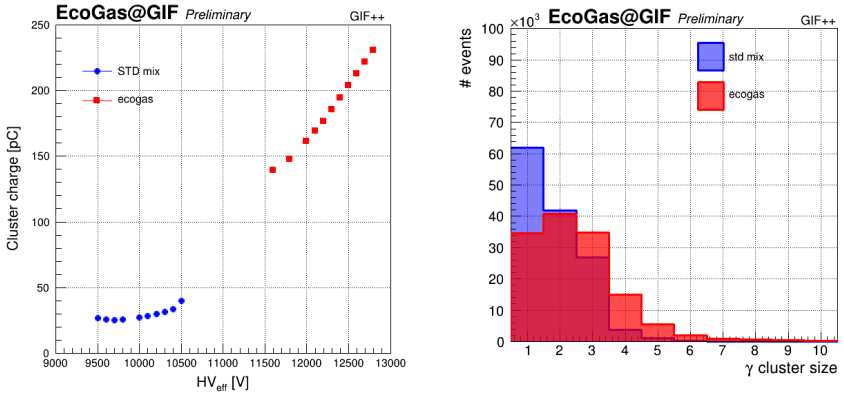

Figure 16: Left: CMS RPC average avalanche charge versus the effective high voltage, measured in presence of gamma background, using the standard gas mixture (blue) and using the ecogas mixture (red). Right: CMS RPC average gamma cluster size distribution measured using the standard gas mixture (blue) and using the ecogas mixture (red).

3.2 Longevity test at GIF++ using eco-friendly gas mixture

The detectors irradiation test is recently started at GIF++ to study the RPC longevity when operating with the ecogas mixture. All the five chambers have been irradiated at $\approx 800\ Hz/cm^2$ as gamma background rate measured at working point, operating with 1 gas volume exchange per hour.

Figure 17 (left) shows the ohmic current of the the CMS RPC chamber, measured at 6 kV, as a function of time. The ohmic current increased in all the chambers, and after two weeks of irradiation it was around 4 times higher than the initial one. It was therefore decided to stop the irradiation and just flush the chambers with fresh gas. The ohmic current decreased, up to reduce a factor ≈ 2 after two weeks. The irradiation was then restarted, and after 1 week the currents were already at the same level measured before the irradiation stop, or even higher in some gaps. Further investigation to mitigate the irradiation effect are ongoing.

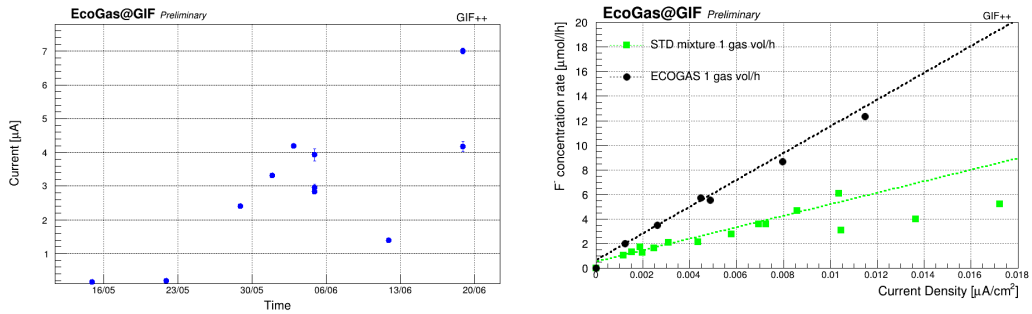

Figure 17: Left: ohmic currents of CMS RPC chamber, measured at 6 kV, monitored as a function of the time. Right: fluoride concentration rate as a function of the background current, measured operating the CMS RPC chamber with 1 gas volume exchange per hour of standard mixture (green) or ecogas mixture (black).

The HFO molecules, as the $C_2H_2F_4$, can be broken under the effects of radiation and electric field, generating fluorine ions and then HF. Therefore, the HF production using the ecogas mixture was studied for the CMS RPC chamber, with particular attention because the HF could be the possible cause of the observed dark current increase. The results are reported in Figure 17 (right), which shows the HF concentration rate as a function of the background current, measured operating the CMS RPC chamber with 1 gas volume exchange per hour of standard mixture (green) or ecogas mixture (black).

The HF concentration in the ecogas mixture is around 2.5 times greater than the standard

gas mixture. This can also be understood by the fact that HFOs have a very short atmospheric lifetime, which indeed gives the low GWP value, but on the other hand they decompose easier than $C_2H_2F_4$.

The Fluoride measurements highlight that if HFOs will be used during HL-LHC, the accumulation of HF will be higher with respect to $C_2H_2F_4$, with the consequent possible effects on the detector longevity.

Further tests to fine-tune the gas component fractions are needed to find the best compromise between the detector performance and longevity.

4 L1 Muon trigger study

The CMS L1 trigger system is responsible for selecting 10^5 interesting events for physics studies out of 40 million proton-proton collisions occurring every second at the LHC [19].

The L1 trigger consists of two parts: the muon trigger and the calorimeter trigger, which both send data to the Global Trigger (GT).

The upgraded L1 Muon Trigger for Run II is composed of three separate Muon Track Finders (MTF) covering different η regions [20]. The Barrel Muon Track Finder (BMTF) receives data from DT and RPC detectors, and covers the $|\eta| < 0.83$. The Endcap Muon Track Finder (EMTF) receives data from RPC and CSC in the region $|\eta| > 1.24$. Finally, the Overlap Muon Track Finder (OMTF) receives data from the three subdetectors in the intermediate region $0.83 < |\eta| < 1.24$.

In the barrel region the muon primitives are sent to the TwinMux, which is a preprocessor layer for the track finder. At this level the RPC hits in adjacent strips are clusterized into a single Trigger Primitve (TP). The DT TP are built in each Super Layer (LS) based on the combination of the 4 single DT layers, and a quality marker is assigned.

The TwinMux combines the TP from DT and RPC, to generate better quality candidates, called superprimitives (SP). If the DT TP have both inner and outer DT layers, then the RPC information are not used. While the RPC information are used to correct the bunch-crossing when only 1 DT layer is present. Finally, if the DT TP have only 1 low quality layer or no DT TP is found, then the algorithm tries to build an RPC only segment in the first two stations by correlating the two RPC layers. The position is given by the average angular position (ϕ) of the two clusters in a temporal coincidence and a bending angle (ϕ_b) given by:

$$\phi_b = arctan(\frac{x_2 - x_1}{D} - \phi) \tag{5}$$

where x_1 and x_2 are the cluster positions and D is the distance between the two RPC layers.

TwinMux is finally in charge of sending the SP to the BMTF and to the OMTF. The BMTF uses the TwinMux data to reconstruct muon tracks and calculate the physical parameters, which are the transverse momentum, the ϕ and η angles, the quality of the candidate and the track addresses.

The OMTF combines simultaneously DT, RPC, and CSC primitives into single tracks using a Golden Pattern (GP) algorithm. The hit pattern is compared to a limited number of pre-computed hit patterns. The track parameters of the GP closest to the actual hit pattern are chosen. The final result is cleaned for duplicates.

The EMTF uses information from both RPC and CSC. RPC hits are used in case of missing CSC information. The RPC hits are clustered and assigned coordinates (θ, ϕ) by the Concentration Pre-Processing and Fan-out card (CPPF). EMTF compare all track segments to predefined patterns in a region, requiring at least two stations with matches to declare a potential track.

Finally, the output of the three systems is collected by the Global Muon Trigger (μGMT). Each MTF forwards the three best track candidates per 60° sector in ϕ. The μGMT ranks the muons by transverse momentum and quality, removes the reconstruction duplicates across boundary regions, and sends the output muon collection to the Global Trigger (GT).

4.1 Optimization of the RPC cluster size cut for the L1 muon trigger

So far only RPC TP with 3 or less strips have been used at L1 muon trigger. The average RPC cluser size is around 2, nevertheless, a not negligible fraction of TP, around 4%, have cluster size higher than 3. This cut was introduced due to MTF firmware limitations in the clustering algorithm, but was never optimized.

In view of the next runs, the RPC information usage at the L1 muon trigger has been optimized. In particular, a study to optimize the RPC cluster size cut was performed taking into account all the relevant factors such as: the RPC spatial resolution, the RPC TP rate, the RPC muon hit efficiency, and finally the MTF trigger rate and efficiency. For the study the 2018 Single muon dataset has been used, and the cluster size cut operated by the CPPF and TwinMux has been emulated.

The RPC spatial resolution has been estimated using the segment extrapolation algorithm, where an high quality DT/CSC segment associated to a stand-alone muon track is extrapolated to the RPC strip plane [21]. The spatial resolution is quantified by the standard deviation (σ) of the residuals distribution between the expected hit position ($\phi_{RPC\ hit\ projected}$) and the reconstructed hit position ($\phi_{RPC\ hit}$):

$$\sigma = \phi_{RPC\ hit\ projected} - \phi_{RPC\ hit} \tag{6}$$

Figure 18 shows the RPC spatial resolution in ϕ coordinate, for both barrel and endcap, as a function of the cluster size cut (left) and the cluster size (right).

The plot in Figure 18 (left) shows that, in both barrel and endcap, the spatial resolution remains almost constant and it is not significantly degraded when the cluster size cut is relaxed. This because the relative fraction of hits introduced by relaxing the cluster size cut is small, and because the spatial resolution of the TP having cluster size greater than 3 is not degraded, as reported in Figure 18 (right). It must be specified that in the right plot, the point at cluster size 6 includes all the events having cluster size equal or greater than 6, and the statistical error is huge due to the low amount of events. The same goes for the left plot, where the last point includes all the TP and no any cluster size cut is applied.

The slightly different resolution between barrel and endcap is due to the different strip pitch, slightly finer in the latter.

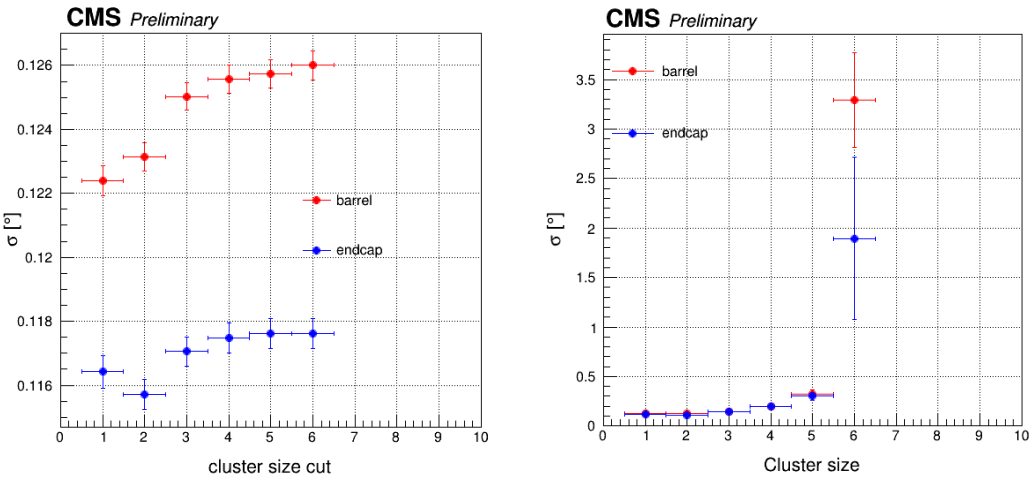

Figure 18: Spatial resolution of the RPC TP in barrel (red) and endcap (blue), as a function of the cluster size cut (letf) and cluster size (right).

Figure 19 (left) shows the distribution of the RPC TP sent by the endcap CPPF to the EMTF as a function of the cluster size cut. The TP slightly increases when the cluster size cut is relaxed, but does not diverge. In particular, the TP increases of ≈3% applying a cluster size 4 instead of 3.

Figure 19 (right) shows the distribution of the SP generated by the barrel TwinMux as a function of the cluster size cut. In yellow is reported the total amount of SP, which slightly increases when the RPC cluster size cut is relaxed. In particular the SP increases of ≈0.2% applying a cluster size 4 instead of 3. The cut relaxation has less impact with respect to the endcap, since in the barrel around 92% of the SP are generated by the DT only.

The contribute of the different SP types are reported as well. A slight decrease of ≈ 0.1% is observed for the SP that use only DT data, identified as "rpc bit-0", when the RPC cluster size cut is relaxed at 4. The decrease is explained by the fact that a fraction of SP used DT only because the RCP TP was not accepted due to the higher cluster size, while they can be used when the cluster size cut is relaxed. Indeed, the number of SP "rpc bit-1" slightly increases of ≈ 0.1%. Finally, the SP "rpc bit2", that represents the RPC only, increases of ≈ 7% applying a cluster size 4 instead of 3. As expected the main impact of the cluster size cut relaxation is for the SP RPC only, nevertheless, these SP represent just the 3% of the total SP amount.

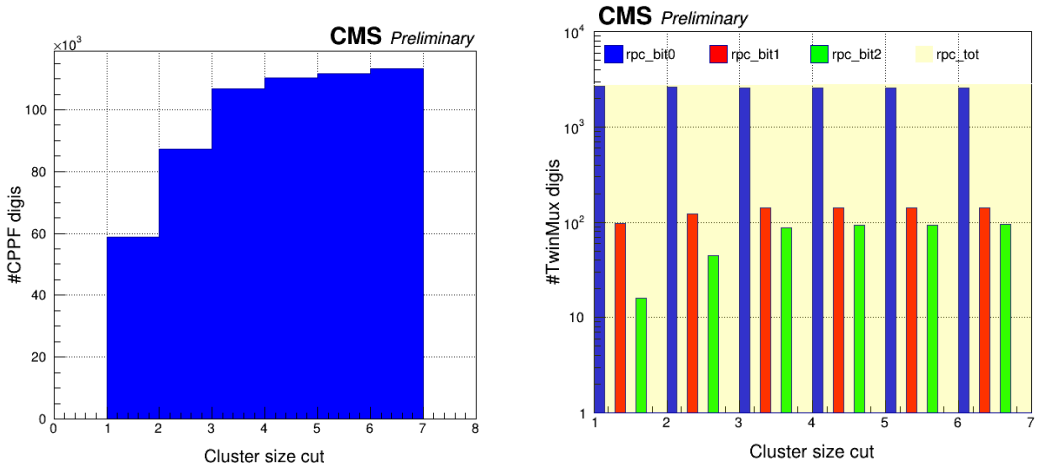

Figure 19: Distribution of the TP as a function of the cluster size cut, in the edcap CPPF (left) and barrel TwinMux (right). For the barrel the contribute of the different TP types is reported: rpc-bit0, rpc-bit1 and rpc-bit2.

All the results reported demonstrate that the cluster size cut relaxation would not have any significant impact on the data transmission.

Concerning the efficiency, the RPC muon hit efficiency increase is significant when the relaxation of the cluster size cut is applied. In particular, the efficiency raises of $\approx 2\%$ in the barrel when the cluster size cut is increased at 4, and $\approx 4\%$ in the endcap.

Finally, the impact of the cluster size cut on the MTF trigger rate and efficiency has been performed using the tag-and-probe method based on the re-emulation of MTF algorithms. The efficiencies simulated in the three MTF applying different cluster size cut are reported as a function of the p_T in Figure 20. Relaxing the RPC cluster size cut has a small but positive impact on muon efficiency, especially at high p_T. In particular, the muon efficiency raises up to 0.5% in the OTMF when a cluster size cut at 4 is applied. The MTF muon trigger rate remains stable when the RPC cluster size cut is relaxed.

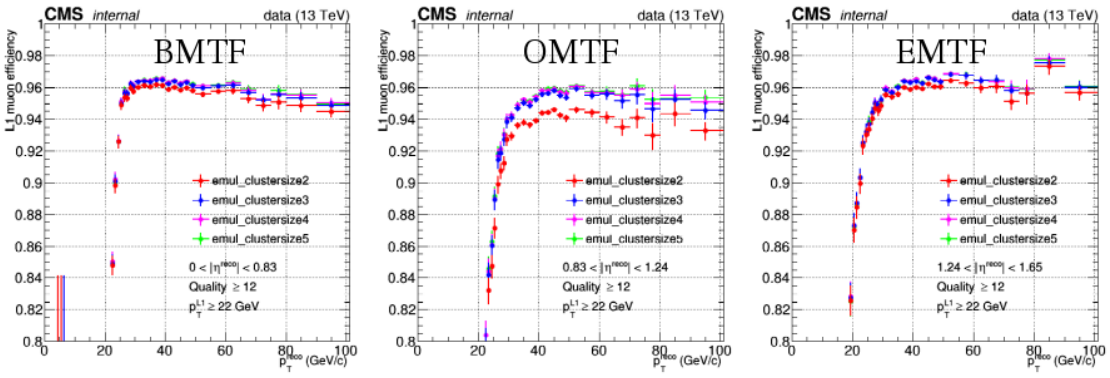

Figure 20: MTF efficiency as a function of p_T,applying different RPC cluster size cuts. The results are shown for the three regions: BMTF (left), OMTF (center) and EMTF (right).

In conclusion, the study proved that increasing the RPC cluster size cut from 3 to 4, neither would affect the spatial resolution, nor the TP rate, but the RPC muon hit efficiency would increase. Finally, the MTF efficiency have a small but positive increase, without any significant increase in the muon trigger rate.

The study lead to the OMTF community to decided to apply the cluster size cut 4 in the future runs, while in the BMTF and EMTF community the discussion is ongoing to evaluate the impact at the firmware level.

[1] The CMS Collaboration, "The CMS muon project: Technical Design Report",Technical Design Report CMS, CERN-LHCC-97-032. CERN, Geneva, 1997.

[2] G. Pugliese, The CMS Muon Collaboration,"The RPC system for the CMS experiment", 2006 IEEE NSS Conference Record N24-3, Jan (2007).

[3] CMS Collaboration, "The Phase-2 Upgrade of the CMS Muon Detectors", CERN-LHCC-2017-012. CMS-TDR-016, 2017.

[4] G. Pugliese et al., "Long-term performance of double gap resistive plate chambers under gamma irradiation", Nuclear Instruments and Methods in Physics Research A 477, 2002.

[5] CMS Collaboration, "CMS RPC system operation and performance during LHC Run II data-taking", to be submitted, 2019.

[6] R. Guida et al., "HF production in CMS-Resistive Plate Chambers", Nuclear Instruments and Methods in Physics Research, 2006.

[7] R. Guida [EN and EP and AIDA GIF++ Collaborations], "GIF++: A new CERN Irradiation Facility to test large-area detectors for the HL-LHC program", PoS ICHEP2016, 2016.

[8] A. Gelmi et al. [CMS Muon Collaboration & CERN EP-DT group], "Fluoride production in CMS Resistive Plate Chambers and aging study", PoS EPS HEP2019, 2019.

[9] A. Gelmi et al. [CMS Muon collaboration], "Longevity studies on the CMS-RPC system", Journal of Instrumentation, 2018.

[10] A. Gelmi et al. [CMS Muon collaboration], "Long-term aging studies on Resistive Plate Chambers (RPC) of the CMS muon system for HL-LHC", IEEE Xplore, 2018.

[11] G. Aielli et al., "Further advances in aging studies for RPCs", Nuclear Instruments and Methods in Physics Research A, 2003.

[12] K. S. Lee et al., "Radiation tests of real-sized prototype RPCs for the Phase-2 Upgrade of the CMS Muon System", JINST, 2016.

[13] K.Shchablo et al., "Performance of the CMS RPC upgrade using 2D fast timing readout system", Nuclear Instruments and Methods in Physics Research Section A, 2019.

[14] A. Gelmi et. al [CMS Muon collaboration], "Background rate study for the CMS improved-RPC at HL-LHC using GEANT4", Nuclear Instruments and Methods in Physics Research Section, 2019.

[15] The European Parliament and the Council of the European Union, "Regulation (EU) No 517/2014 of 16 April 2014 on fluorinated greenhouse gases", technical report, EU, 2014.

[16] J.S. Brown, "HFOs new low global warming potential refrigerant", ASHRAE J., 2009.

[17] L. Benussi et al., "A study of HFO-1234ze (1,3,3,3-Tetrafluoropropene) as an eco-friendly replacement in RPC detectors", 2015. arXiv:1505.01648 [physics.ins-det].

[18] G. Rigoletti et al. [Ecogas Collaboration], "Studies of RPC operations with ecological gas mixture under irradiation at GIF++", EPS 2019 proceeding submitted.

[19] A. Tapper et al. [CMS Collaboration], "CMS Technical Design Report for the Level-1 Trigger Upgrade", CERN-LHCC-2013-011. CMS-TDR-12, 2013.

[20] A. Tapper [CMS Collaboration], "The CMS Level-1 Trigger for LHC Run II", PoS, 2017.

[21] CMS collaboration, "Muon Reconstruction in the CMS Detector", CMS AN 2008/097, 2009.

5 Schools and Conferences

- XIV Seminar on Software for Nuclear, Subnuclear and Applied Physics, Alghero, Italy, June 2017
- CMS Physics Object School POS, Bari, Italy, September 2017, participating as facilitator and giving a lesson about the introduction of GEANT4 and a short exercise
- RD51 Gaseous detectors lectures, 11-15 December 2017, CERN, Switzerland
- First International RPC detector school, 14-17 February 2018, Mexico City, Mexico
- XXX National seminar of nuclear and subnuclear physics, 5-12 June 2018, Otranto, Italy
- CMS Machine Learning workshop, 2-4 July 2018, CERN, Switzerland
- International School Of Trigger and Data AcQuisition (ISOTDAQ), London (UK), 3-12 April 2019.

6 Conferences

- Congresso nazionale societa italiana di fisica SIF2017, September 2017, Trento, Italy
  Oral presentation: *"Upgrade of the RPC system of the CMS Muon Spectrometer"*
- 2017 Fall Meeting of the Korean Physical Society, October 2017, Gyeongju-si, Korea
  Oral presentation: *"Upgrade of the RPC system of the CMS Muon Spectrometer"*
- XIV Workshop on Resistive Plate Chambers and Related Detectors (RPC 2018), 19-23 February 2018, Puerto Vallarta, Mexico
  Oral presentation: *"Longevity studies for the CMS-RPC system"*
- Incontri di Fisica dele Alte Energie IFAE 2018, 4-6 April 2018, Milano, Italy
  Oral presentation: *"RPC upgrade project for CMS Phase II"*
- 14th Pisa Meeting on Advanced Detectors PM2018, 27 May - 2 June 2018, La Biodola, Isola d'Elba, Italy
  National conference. Poster: *"Background rate study for the CMS improved-RPC at HL-LHC using GEANT4"*
- 2018 IEEE Nuclear Science Symposium and Medical Imaging conference (IEEE 2018), Sydney (Australia), 20-27 November 2018.
  Oral presentation: *"Long-term aging studies on Resistive Plate Chambers (RPC) of the CMS muon system for HL-LHC"*.
- Students' Poster Session at the 2019 Winter LHCC meeting (Posters@LHCC), CERN, 27 February 2019.
  Poster: *"improved-RPC for the CMS muon spectrometer upgrade for HL-LHC"*.
- European Physical Society Conference on High Energy Physics (EPS2019), Ghent (Belgium), 10-17July 2019.
  Oral presentation: *"Fluoride production in CMS Resistive Plate Chambers (RPC) and aging studies"*.

7 Publications

7.1 First author pubblications

- A. Gelmi et al. [CMS Muon collaboration], **"Longevity studies on the CMS-RPC system"**, Journal of Instrumentation, 2018.
- A. Gelmi et. al [CMS Muon collaboration], **"Background rate study for the CMS improved-RPC at HL-LHC using GEANT4"**, Nuclear Instruments and Methods in Physics Research Section, 2019. doi.org/10.1016/j.nima.2018.10.046.
- A. Gelmi et al. [CMS Muon collaboration], **"Long-term aging studies on Resistive Plate Chambers (RPC) of the CMS muon system for HL-LHC"**, IEEE Xplore, 2019.
- A. Gelmi et al. [CMS Muon collaboration & CERN-EP-DT group], **"Fluoride production in CMS Resistive Plate Chambers (RPC) and aging studies"**, EPS 2019 proceeding submitted.

7.2 RPC group & Ecogas Collaboration publications

- "RPC upgrade project for CMS Phase II", M.I. Pedraza et al., [CMS RPC group], JINST, 2018.
- "R&D results of iRPC tested at GIF++ for CMS Phase II upgrade", J. H. Lim et al., [CMS RPC group], JINST, 2018.
- "Fast timing measurement for CMS RPC Phase II upgrade", C. Combaret et al., [CMS RPC group], JINST, 2018.
- "RPC Radiation Background Simulations for the High Luminosity Phase in the CMS Experiment", B. Carpinteyro et al., [CMS RPC group], JINST, 2018.
- "CMS RPC background studies during LHC run II", R. Trejo et al., [CMS RPC group], JINST, 2018.
- "High rate, high time precision RPC detector for LHC", F. Lagarde et al., [CMS RPC group], JINST, 2018.
- "The CMS RPC Detector Status and Operation at LHC", M.Shah et al., [CMS RPC group], JINST, 2018.
- "Test of a real-size Mosaic MRPC developed for CMS muon upgrade", Y. Yu et al., [CMS RPC group], JINST, 2018.
- "CMS RPC efficiency measurement using the Tag and Probe method", J. Goh et al., [CMS RPC group], JINST, 2018.
- "CMS RPC Integrated Charge", M. Cecilia et al., [CMS RPC group], JINST, 2018.
- "The CMS RPC system calibration", R. Reyes et al., [CMS RPC group], JINST, 2018.
- "RE3/1 and RE4/1 chambers integration with Forward region of CMS Muon spectrometer", E. Voevodina et al., [CMS RPC group], JINST, 2018.
- "CMS RPC Condition Data Automation", O. M. Colin et al., [CMS RPC group], JINST, 2018.
- "Search for Heavy Stable Charged Particles in the CMS Experiment using the RPC phase II upgraded detectors", G. Sanchez et al., [CMS RPC group], JINST, 2018.
- "CMS RPC system operation and performance during LHC Run II data-taking", CMS Collaboration, to be submitted 2019.
- "Studies of RPC operations with ecological gas mixture under irradiation at GIF++", G. Rigoletti et al. [Ecogas Collaboration], EPS 2019 proceeding submitted.

7.3 CMS Collaboration publications

[1] A. M. Sirunyan *et al.*, "Study of J/ψ meson production from jet fragmentation in pp collisions at $\sqrt{s} = 8$ TeV," 2019.

[2] A. M. Sirunyan *et al.*, "Search for supersymmetry with a compressed mass spectrum in events with a soft τ lepton, a highly energetic jet, and large missing transverse momentum in proton-proton collisions at $\sqrt{s} = 13$ TeV," 2019.

[3] A. M. Sirunyan *et al.*, "Calibration of the CMS hadron calorimeters using proton-proton collision data at $\sqrt{s} = 13$ TeV," 2019.

[4] A. M. Sirunyan *et al.*, "Running of the top quark mass from proton-proton collisions at $\sqrt{s} = 13$ TeV," 2019.

[5] A. M. Sirunyan *et al.*, "Search for long-lived particles using delayed photons in proton-proton collisions at $\sqrt{s} = 13$ TeV," 2019.

[6] A. M. Sirunyan *et al.*, "Evidence for WW production from double-parton interactions in proton-proton collisions at $\sqrt{s} = 13$ TeV," 2019.

[7] A. M. Sirunyan *et al.*, "Measurement of the $\mathrm{t\bar{t}b\bar{b}}$ production cross section in the all-jet final state in pp collisions at $\sqrt{s} = 13$ TeV," 2019.

[8] A. M. Sirunyan *et al.*, "Search for electroweak production of a vector-like T quark using fully hadronic final states," 2019.

[9] A. M. Sirunyan *et al.*, "Measurements of differential Z boson production cross sections in proton-proton collisions at $\sqrt{s} = 13$ TeV," 2019.

[10] A. M. Sirunyan *et al.*, "Search for low mass vector resonances decaying into quark-antiquark pairs in proton-proton collisions at $\sqrt{s} = 13$ TeV," 2019.

[11] A. M. Sirunyan *et al.*, "Searches for physics beyond the standard model with the M_{T2} variable in hadronic final states with and without disappearing tracks in proton-proton collisions at $\sqrt{s} = 13$ TeV," 2019.

[12] A. M. Sirunyan *et al.*, "Search for a charged Higgs boson decaying into top and bottom quarks in proton-proton collisions at $\sqrt{s} = 13$ TeV in events with electrons or muons," 2019.

[13] A. M. Sirunyan *et al.*, "Search for supersymmetry using Higgs boson to diphoton decays at $\sqrt{s} = 13$ TeV," 2019.

[14] A. M. Sirunyan *et al.*, "Search for production of four top quarks in final states with same-sign or multiple leptons in proton-proton collisions at $\sqrt{s} = 13$ TeV," 2019.

[15] A. M. Sirunyan *et al.*, "Search for supersymmetry in proton-proton collisions at 13 TeV in final states with jets and missing transverse momentum," 2019.

[16] A. M. Sirunyan *et al.*, "Search for dark photons in decays of Higgs bosons produced in association with Z bosons in proton-proton collisions at $\sqrt{s} = 13$ TeV," 2019.

[17] A. M. Sirunyan *et al.*, "Search for dark matter particles produced in association with a Higgs boson in proton-proton collisions at $\sqrt{s} = 13$ TeV," 2019.

[18] A. M. Sirunyan *et al.*, "Measurement of the average very forward energy as a function of the track multiplicity at central pseudorapidities in proton-proton collisions at $\sqrt{s} = 13$ TeV," 2019.

[19] A. M. Sirunyan *et al.*, "Search for heavy Higgs bosons decaying to a top quark pair in proton-proton collisions at $\sqrt{s} = 13$ TeV," 2019.

[20] A. M. Sirunyan *et al.*, "Search for anomalous triple gauge couplings in WW and WZ production in lepton + jet events in proton-proton collisions at $\sqrt{s} = 13$ TeV," 2019.

[21] A. M. Sirunyan *et al.*, "Measurement of differential cross sections and charge ratios for t-channel single top quark production in proton-proton collisions at $\sqrt{s} = 13$ TeV," 2019.

[22] A. M. Sirunyan *et al.*, "Measurements of triple-differential cross sections for inclusive isolated-photon+jet events in pp collisions at $\sqrt{s} = 8$ TeV," 2019.

[23] A. M. Sirunyan *et al.*, "Search for light pseudoscalar boson pairs produced from decays of the 125 GeV Higgs boson in final states with two muons and two nearby tracks in pp collisions at $\sqrt{s} = 13$ TeV," 2019.

[24] A. M. Sirunyan *et al.*, "Search for physics beyond the standard model in events with overlapping photons and jets," 2019.

[25] A. M. Sirunyan *et al.*, "Study of the $\mathrm{B}^+ \to \mathrm{J}/\psi\overline{\Lambda}\mathrm{p}$ decay in proton-proton collisions at $\sqrt{s} = 8$ TeV," 2019.

[26] A. M. Sirunyan *et al.*, "Measurement of the top quark polarization and $\mathrm{t\bar{t}}$ spin correlations using dilepton final states in proton-proton collisions at $\sqrt{s} = 13$ TeV," 2019.

[27] A. M. Sirunyan *et al.*, "Search for MSSM Higgs bosons decaying to $\mu^+\mu^-$ in proton-proton collisions at $\sqrt{s} = 13$ TeV," 2019.

[28] A. M. Sirunyan *et al.*, "Measurement of the top quark Yukawa coupling from $\mathrm{t\bar{t}}$ kinematic distributions in the lepton+jets final state in proton-proton collisions at $\sqrt{s} = 13$ TeV," 2019.

[29] A. M. Sirunyan *et al.*, "Combined search for supersymmetry with photons in proton-proton collisions at $\sqrt{s} = 13$ TeV," 2019.

[30] A. M. Sirunyan *et al.*, "Search for pair production of vector-like quarks in the fully hadronic final state," *Phys. Rev.*, vol. D100, p. 072001, 2019.

[31] A. M. Sirunyan *et al.*, "Search for long-lived particles using nonprompt jets and missing transverse momentum with proton-proton collisions at $\sqrt{s} = 13$ TeV," *Phys. Lett.*, vol. B797, p. 134876, 2019.

[32] A. M. Sirunyan *et al.*, "A multi-dimensional search for new heavy resonances decaying to boosted WW, WZ, or ZZ boson pairs in the dijet final state at 13 TeV," 2019.

[33] A. M. Sirunyan *et al.*, "Production of Λ_c^+ baryons in proton-proton and lead-lead collisions at $\sqrt{s_\mathrm{NN}} = 5.02$ TeV," 2019.

[34] A. M. Sirunyan *et al.*, "Search for the Production of Four Top Quarks in the Single-Lepton and Opposite-Sign Dilepton Final States in Proton-Proton Collisions at $\sqrt{s} = 13$ TeV," 2019.

[35] A. M. Sirunyan *et al.*, "Combination of CMS searches for heavy resonances decaying to pairs of bosons or leptons," *Phys. Lett.*, vol. B798, p. 134952, 2019.

[36] A. M. Sirunyan *et al.*, "Search for supersymmetry with a compressed mass spectrum in the vector boson fusion topology with 1-lepton and 0-lepton final states in proton-proton collisions at $\sqrt{s} = 13$ TeV," *JHEP*, vol. 08, p. 150, 2019.

[37] A. M. Sirunyan *et al.*, "Search for vector-like leptons in multilepton final states in proton-proton collisions at $\sqrt{s} = 13$ TeV," *Phys. Rev.*, vol. D100, no. 5, p. 052003, 2019.

[38] A. M. Sirunyan *et al.*, "Search for Higgs and Z boson decays to J/ψ or Υ pairs in proton-proton collisions at $\sqrt{s} = 13$ TeV," 2019.

[39] A. M. Sirunyan *et al.*, "Search for low-mass quark-antiquark resonances produced in association with a photon at $\sqrt{s} = 13$ TeV," 2019.

[40] A. M. Sirunyan *et al.*, "Correlations of azimuthal anisotropy Fourier harmonics in pPb collisions at $\sqrt{s_{\mathrm{NN}}} = 8.16$ TeV," 2019.

[41] A. M. Sirunyan *et al.*, "Search for anomalous electroweak production of vector boson pairs in association with two jets in proton-proton collisions at 13 TeV," *Phys. Lett.*, vol. B798, p. 134985, 2019.

[42] A. M. Sirunyan *et al.*, "Search for a light charged Higgs boson decaying to a W boson and a CP-odd Higgs boson in final states with e$\mu\mu$ or $\mu\mu\mu$ in proton-proton collisions at $\sqrt{s} = 13$ TeV," *Phys. Rev. Lett.*, vol. 123, no. 13, p. 131802, 2019.

[43] A. M. Sirunyan *et al.*, "Search for the production of $\mathrm{W^{\pm}W^{\pm}W^{\mp}}$ events at $\sqrt{s} = 13$ TeV," *Phys. Rev.*, vol. D100, no. 1, p. 012004, 2019.

[44] A. M. Sirunyan *et al.*, "Observation of nuclear modifications in $\mathrm{W^{\pm}}$ boson production in pPb collisions at $\sqrt{s_{\mathrm{NN}}} = 8.16$ TeV," 2019.

[45] A. M. Sirunyan *et al.*, "Multiparticle correlation studies in pPb collisions at $\sqrt{s_{\mathrm{NN}}} = 8.16$ TeV," 2019.

[46] A. M. Sirunyan *et al.*, "Measurement of $\mathrm{t\bar{t}}$ normalised multi-differential cross sections in pp collisions at $\sqrt{s} = 13$ TeV, and simultaneous determination of the strong coupling strength, top quark pole mass, and parton distribution functions," *Submitted to: Eur. Phys. J.*, 2019.

[47] A. M. Sirunyan *et al.*, "Search for resonances decaying to a pair of Higgs bosons in the $\mathrm{b\bar{b}q\bar{q}'}\ell\nu$ final state in proton-proton collisions at $\sqrt{s} = 13$ TeV," *Submitted to: JHEP*, 2019.

[48] A. M. Sirunyan *et al.*, "Extraction and validation of a new set of CMS PYTHIA8 tunes from underlying-event measurements," 2019.

[49] A. M. Sirunyan *et al.*, "Search for new physics in top quark production in dilepton final states in proton-proton collisions at $\sqrt{s} = 13$ TeV," 2019.

[50] A. M. Sirunyan *et al.*, "Search for a low-mass $\tau^+\tau^-$ resonance in association with a bottom quark in proton-proton collisions at $\sqrt{s} = 13$ TeV," *JHEP*, vol. 05, p. 210, 2019.

[51] A. M. Sirunyan *et al.*, "Search for supersymmetry in final states with photons and missing transverse momentum in proton-proton collisions at 13 TeV," *JHEP*, vol. 06, p. 143, 2019.

[52] A. M. Sirunyan *et al.*, "Constraints on anomalous HVV couplings from the production of Higgs bosons decaying to τ lepton pairs," *Submitted to: Phys. Rev.*, 2019.

[53] A. M. Sirunyan *et al.*, "Performance of missing transverse momentum reconstruction in proton-proton collisions at $\sqrt{s} = 13$ TeV using the CMS detector," *JINST*, vol. 14, no. 07, p. P07004, 2019.

[54] A. M. Sirunyan *et al.*, "Search for charged Higgs bosons in the $\mathrm{H^{\pm}} \to \tau^{\pm}\nu_{\tau}$ decay channel in proton-proton collisions at $\sqrt{s} = 13$ TeV," *JHEP*, vol. 07, p. 142, 2019.

[55] A. M. Sirunyan *et al.*, "Measurement of electroweak production of a W boson in association with two jets in proton-proton collisions at $\sqrt{s} = 13$ TeV," 2019.

[56] A. M. Sirunyan *et al.*, "An embedding technique to determine $\tau\tau$ backgrounds in proton-proton collision data," *JINST*, vol. 14, no. 06, p. P06032, 2019.

[57] A. M. Sirunyan *et al.*, "Search for a heavy pseudoscalar boson decaying to a Z and a Higgs boson at $\sqrt{s} = 13$ TeV," *Eur. Phys. J.*, vol. C79, no. 7, p. 564, 2019.

[58] M. Aaboud *et al.*, "Combinations of single-top-quark production cross-section measurements and $|f_{\mathrm{LV}}V_{tb}|$ determinations at $\sqrt{s} = 7$ and 8 TeV with the ATLAS and CMS experimentsCombinations of single-top-quark production cross-section measurements and —$\mathrm{f}_{LV}\mathrm{V}_{tb}$— determinations at $\sqrt{s} = 7$ and 8 TeV with the ATLAS and CMS experiments," *JHEP*, vol. 05, p. 088, 2019.

[59] A. M. Sirunyan *et al.*, "Azimuthal separation in nearly back-to-back jet topologies in inclusive 2- and 3-jet events in pp collisions at $\sqrt{s} = 13$ TeV," *Eur. Phys. J.*, vol. C79, no. 9, p. 773, 2019.

[60] A. M. Sirunyan *et al.*, "Pseudorapidity distributions of charged hadrons in xenon-xenon collisions at $\sqrt{s_{\mathrm{NN}}} = 5.44$ TeV," 2019.

[61] A. M. Sirunyan *et al.*, "Measurement of exclusive $\rho(770)^0$ photoproduction in ultraperipheral pPb collisions at $\sqrt{s_{\mathrm{NN}}} = 5.02$ TeV," *Eur. Phys. J.*, vol. C79, no. 8, p. 702, 2019.

[62] A. M. Sirunyan *et al.*, "Observation of Two Excited $\mathrm{B_c^+}$ States and Measurement of the $\mathrm{B_c^+}$(2S) Mass in pp Collisions at $\sqrt{s} = 13$ TeV," *Phys. Rev. Lett.*, vol. 122, no. 13, p. 132001, 2019.

[63] A. M. Sirunyan *et al.*, "Search for W boson decays to three charged pions," *Phys. Rev. Lett.*, vol. 122, no. 15, p. 151802, 2019.

[64] A. M. Sirunyan *et al.*, "Charged-particle angular correlations in XeXe collisions at $\sqrt{s_{\mathrm{NN}}} = 5.44$ TeV," *Phys. Rev.*, vol. C100, no. 4, p. 044902, 2019.

[65] A. M. Sirunyan *et al.*, "Search for supersymmetry in events with a photon, jets, b -jets, and missing transverse momentum in protonproton collisions at 13 TeV," *Eur. Phys. J.*, vol. C79, no. 5, p. 444, 2019.

[66] A. M. Sirunyan *et al.*, "Measurement of electroweak WZ boson production and search for new physics in WZ + two jets events in pp collisions at $\sqrt{s} = 13$TeV," *Phys. Lett.*, vol. B795, pp. 281–307, 2019.

[67] A. M. Sirunyan *et al.*, "Measurements of the pp $\rightarrow$ WZ inclusive and differential production cross section and constraints on charged anomalous triple gauge couplings at $\sqrt{s} = 13$ TeV," *JHEP*, vol. 04, p. 122, 2019.

[68] A. M. Sirunyan *et al.*, "Search for dark matter produced in association with a single top quark or a top quark pair in proton-proton collisions at $\sqrt{s} = 13$ TeV," *JHEP*, vol. 03, p. 141, 2019.

[69] A. M. Sirunyan *et al.*, "Search for the pair production of light top squarks in the $\mathrm{e}^{\pm}\mu^{\mp}$ final state in proton-proton collisions at $\sqrt{s} = 13$ TeV," *JHEP*, vol. 03, p. 101, 2019.

[70] A. M. Sirunyan *et al.*, "Measurements of the Higgs boson width and anomalous HVV couplings from on-shell and off-shell production in the four-lepton final state," *Phys. Rev.*, vol. D99, no. 11, p. 112003, 2019.

[71] A. M. Sirunyan *et al.*, "Measurement of the single top quark and antiquark production cross sections in the t channel and their ratio in proton-proton collisions at $\sqrt{s} = 13$ TeV," 2018.

[72] A. M. Sirunyan *et al.*, "Measurement of the top quark mass in the all-jets final state at $\sqrt{s} = 13$ TeV and combination with the lepton+jets channel," *Eur. Phys. J.*, vol. C79, no. 4, p. 313, 2019.

[73] A. M. Sirunyan *et al.*, "Measurement of the $\mathrm{t\bar{t}}$ production cross section, the top quark mass, and the strong coupling constant using dilepton events in pp collisions at $\sqrt{s} = 13$ TeV," *Eur. Phys. J.*, vol. C79, no. 5, p. 368, 2019.

[74] A. M. Sirunyan *et al.*, "Measurement of the differential Drell-Yan cross section in proton-proton collisions at $\sqrt{s} = 13$ TeV," *Submitted to: JHEP*, 2018.

[75] A. M. Sirunyan *et al.*, "Search for contact interactions and large extra dimensions in the dilepton mass spectra from proton-proton collisions at $\sqrt{s} = 13$ TeV," *JHEP*, vol. 04, p. 114, 2019.

[76] A. M. Sirunyan *et al.*, "Search for vector-like quarks in events with two oppositely charged leptons and jets in proton-proton collisions at $\sqrt{s} = 13$ TeV," *Eur. Phys. J.*, vol. C79, no. 4, p. 364, 2019.

[77] A. M. Sirunyan *et al.*, "Search for a heavy resonance decaying to a top quark and a vector-like top quark in the lepton+jets final state in pp collisions at $\sqrt{s} = 13$ TeV," *Eur. Phys. J.*, vol. C79, no. 3, p. 208, 2019.

[78] A. M. Sirunyan *et al.*, "Measurement and interpretation of differential cross sections for Higgs boson production at $\sqrt{s} = 13$ TeV," *Phys. Lett.*, vol. B792, pp. 369–396, 2019.

[79] A. M. Sirunyan *et al.*, "Inclusive search for supersymmetry in pp collisions at $\sqrt{s} = 13$ TeV using razor variables and boosted object identification in zero and one lepton final states," *JHEP*, vol. 03, p. 031, 2019.

[80] A. M. Sirunyan *et al.*, "Search for an exotic decay of the Higgs boson to a pair of light pseudoscalars in the final state with two muons and two b quarks in pp collisions at 13 TeV," *Phys. Lett.*, vol. B795, pp. 398–423, 2019.

[81] A. M. Sirunyan *et al.*, "Observation of Single Top Quark Production in Association with a Z Boson in Proton-Proton Collisions at $\sqrt{s}$ =13 TeV," *Phys. Rev. Lett.*, vol. 122, no. 13, p. 132003, 2019.

[82] A. M. Sirunyan *et al.*, "Measurement of the energy density as a function of pseudo-rapidity in proton-proton collisions at $\sqrt{s} = 13$ TeV," *Eur. Phys. J.*, vol. C79, no. 5, p. 391, 2019.

[83] A. M. Sirunyan *et al.*, "Search for supersymmetry in events with a photon, a lepton, and missing transverse momentum in proton-proton collisions at $\sqrt{s} = 13$ TeV," *JHEP*, vol. 01, p. 154, 2019.

[84] A. M. Sirunyan *et al.*, "Measurement of inclusive very forward jet cross sections in proton-lead collisions at $\sqrt{s_{\mathrm{NN}}} = 5.02$ TeV," *JHEP*, vol. 05, p. 043, 2019.

[85] A. M. Sirunyan *et al.*, "A search for pair production of new light bosons decaying into muons in proton-proton collisions at 13 TeV," *Phys. Lett.*, vol. B796, pp. 131–154, 2019.

[86] A. M. Sirunyan *et al.*, "Measurement of associated production of a W boson and a charm quark in proton-proton collisions at $\sqrt{s} = 13$ TeV," *Eur. Phys. J.*, vol. C79, no. 3, p. 269, 2019.

[87] A. M. Sirunyan *et al.*, "Search for dark matter in events with a leptoquark and missing transverse momentum in proton-proton collisions at 13 TeV," *Phys. Lett.*, vol. B795, pp. 76–99, 2019.

[88] A. M. Sirunyan *et al.*, "Search for resonant production of second-generation sleptons with same-sign dimuon events in proton-proton collisions at $\sqrt{s} = 13$ TeV," *Eur. Phys. J.*, vol. C79, no. 4, p. 305, 2019.

[89] A. M. Sirunyan *et al.*, "Search for associated production of a Higgs boson and a single top quark in proton-proton collisions at $\sqrt{s} =$ TeV," *Phys. Rev.*, vol. D99, no. 9, p. 092005, 2019.

[90] A. M. Sirunyan *et al.*, "Combination of searches for Higgs boson pair production in proton-proton collisions at $\sqrt{s} = 13$ TeV," *Phys. Rev. Lett.*, vol. 122, no. 12, p. 121803, 2019.

[91] A. M. Sirunyan *et al.*, "Search for a standard model-like Higgs boson in the mass range between 70 and 110 GeV in the diphoton final state in proton-proton collisions at $\sqrt{s} =$ 8 and 13 TeV," *Phys. Lett.*, vol. B793, pp. 320–347, 2019.

[92] A. M. Sirunyan *et al.*, "Search for long-lived particles decaying into displaced jets in proton-proton collisions at $\sqrt{s} = 13$ TeV," *Phys. Rev.*, vol. D99, no. 3, p. 032011, 2019.

[93] A. M. Sirunyan *et al.*, "Search for a W boson decaying to a vector-like quark and a top or bottom quark in the all-jets final state," *JHEP*, vol. 03, p. 127, 2019.

[94] A. M. Sirunyan *et al.*, "Measurements of $\mathrm{t\bar{t}}$ differential cross sections in proton-proton collisions at $\sqrt{s} = 13$ TeV using events containing two leptons," *JHEP*, vol. 02, p. 149, 2019.

[95] A. M. Sirunyan *et al.*, "Search for dark matter produced in association with a Higgs boson decaying to a pair of bottom quarks in protonproton collisions at $\sqrt{s} = 13$ TeV," *Eur. Phys. J.*, vol. C79, no. 3, p. 280, 2019.

[96] A. M. Sirunyan *et al.*, "Search for excited leptons in $\ell\ell\gamma$ final states in proton-proton collisions at $\sqrt{s} = 13$ TeV," *JHEP*, vol. 04, p. 015, 2019.

[97] A. M. Sirunyan *et al.*, "Search for pair production of first-generation scalar leptoquarks at $\sqrt{s} = 13$ TeV," *Phys. Rev.*, vol. D99, no. 5, p. 052002, 2019.

[98] A. M. Sirunyan *et al.*, "Search for heavy neutrinos and third-generation leptoquarks in hadronic states of two τ leptons and two jets in proton-proton collisions at $\sqrt{s} = 13$ TeV," *JHEP*, vol. 03, p. 170, 2019.

[99] A. M. Sirunyan *et al.*, "Event shape variables measured using multijet final states in proton-proton collisions at $\sqrt{s} = 13$ TeV," *JHEP*, vol. 12, p. 117, 2018.

[100] A. M. Sirunyan *et al.*, "Search for nonresonant Higgs boson pair production in the $\mathrm{b\bar{b}b\bar{b}}$ final state at $\sqrt{s} = 13$ TeV," *JHEP*, vol. 04, p. 112, 2019.

[101] A. M. Sirunyan *et al.*, "Search for low-mass resonances decaying into bottom quark-antiquark pairs in proton-proton collisions at $\sqrt{s} = 13$ TeV," *Phys. Rev.*, vol. D99, no. 1, p. 012005, 2019.

[102] A. M. Sirunyan *et al.*, "Studies of Beauty Suppression via Nonprompt D^0 Mesons in Pb-Pb Collisions at $Q^2 = 4$ GeV^2," *Phys. Rev. Lett.*, vol. 123, no. 2, p. 022001, 2019.

[103] A. M. Sirunyan *et al.*, "Search for rare decays of Z and Higgs bosons to J/ψ and a photon in proton-proton collisions at $\sqrt{s} = 13$ TeV," *Eur. Phys. J.*, vol. C79, no. 2, p. 94, 2019.

[104] A. M. Sirunyan *et al.*, "Search for new particles decaying to a jet and an emerging jet," *JHEP*, vol. 02, p. 179, 2019.

[105] A. M. Sirunyan *et al.*, "Search for pair-produced three-jet resonances in proton-proton collisions at $\sqrt{s} =$13 TeV," *Phys. Rev.*, vol. D99, no. 1, p. 012010, 2019.

[106] A. M. Sirunyan *et al.*, "Search for resonant $\mathrm{t\bar{t}}$ production in proton-proton collisions at $\sqrt{s} = 13$ TeV," *JHEP*, vol. 04, p. 031, 2019.

[107] A. M. Sirunyan *et al.*, "Centrality and pseudorapidity dependence of the transverse energy density in pPb collisions at $\sqrt{s_{\mathrm{NN}}} = 5.02$ TeV," *Phys. Rev.*, vol. C100, no. 2, p. 024902, 2019.

[108] A. M. Sirunyan *et al.*, "Evidence for light-by-light scattering and searches for axion-like particles in ultraperipheral PbPb collisions at $\sqrt{s_{\mathrm{NN}}} = 5.02$ TeV," *Phys. Lett.*, vol. B797, p. 134826, 2019.

[109] A. M. Sirunyan *et al.*, "Search for top quark partners with charge 5/3 in the same-sign dilepton and single-lepton final states in proton-proton collisions at $\sqrt{s} = 13$ TeV," *JHEP*, vol. 03, p. 082, 2019.

[110] A. M. Sirunyan *et al.*, "Measurement of $\mathrm{B}_{\mathrm{s}}^{0}$ meson production in pp and PbPb collisions at $\sqrt{s_{\mathrm{NN}}} = 5.02$ TeV," *Phys. Lett.*, vol. B796, pp. 168–190, 2019.

[111] A. M. Sirunyan *et al.*, "Observation of prompt J/ψ meson elliptic flow in high-multiplicity pPb collisions at $\sqrt{s_{\mathrm{NN}}} = 8.16$ TeV," *Phys. Lett.*, vol. B791, pp. 172–194, 2019.

[112] A. M. Sirunyan *et al.*, "Search for new physics in final states with a single photon and missing transverse momentum in proton-proton collisions at $\sqrt{s} = 13$ TeV," *JHEP*, vol. 02, p. 074, 2019.

[113] A. M. Sirunyan *et al.*, "Measurement of exclusive Υ photoproduction from protons in pPb collisions at $\sqrt{s_{\mathrm{NN}}} = 5.02$ TeV," *Eur. Phys. J.*, vol. C79, no. 3, p. 277, 2019.

[114] A. M. Sirunyan *et al.*, "Combined measurements of Higgs boson couplings in proton-proton collisions at $\sqrt{s} = 13\,\mathrm{TeV}$," *Eur. Phys. J.*, vol. C79, no. 5, p. 421, 2019.

[115] A. M. Sirunyan *et al.*, "Search for single production of vector-like quarks decaying to a top quark and a W boson in proton-proton collisions at $\sqrt{s} = 13$ TeV," *Eur. Phys. J.*, vol. C79, p. 90, 2019.

[116] A. M. Sirunyan *et al.*, "Jet Shapes of Isolated Photon-Tagged Jets in Pb-Pb and pp Collisions at $\sqrt{s_{\mathrm{NN}}} = 5.02$ TeV," *Phys. Rev. Lett.*, vol. 122, no. 15, p. 152001, 2019.

[117] A. M. Sirunyan *et al.*, "Search for invisible decays of a Higgs boson produced through vector boson fusion in proton-proton collisions at $\sqrt{s} = 13\,\mathrm{TeV}$," *Phys. Lett.*, vol. B793, pp. 520–551, 2019.

[118] A. M. Sirunyan *et al.*, "Search for leptoquarks coupled to third-generation quarks in proton-proton collisions at $\sqrt{s} = 13\,\mathrm{TeV}$," *Phys. Rev. Lett.*, vol. 121, no. 24, p. 241802, 2018.

[119] A. M. Sirunyan *et al.*, "Search for the associated production of the Higgs boson and a vector boson in proton-proton collisions at $\sqrt{s} = 13$ TeV via Higgs boson decays to τ leptons," *JHEP*, vol. 06, p. 093, 2019.

[120] A. M. Sirunyan *et al.*, "Studies of $\mathrm{B}^{*\mathrm{s2}}(5840)^{0}$ and $\mathrm{B}_{\mathrm{s1}}(5830)^{0}$ mesons including the observation of the $\mathrm{B}^{*\mathrm{s2}}(5840)^{0} \to \mathrm{B}^{0}\mathrm{K}_{\mathrm{S}}^{0}$ decay in proton-proton collisions at $\sqrt{s} = 8\,\mathrm{TeV}$," *Eur. Phys. J.*, vol. C78, no. 11, p. 939, 2018.

[121] A. M. Sirunyan *et al.*, "Performance of reconstruction and identification of τ leptons decaying to hadrons and ν_{τ} in pp collisions at $\sqrt{s} = 13$ TeV," *JINST*, vol. 13, no. 10, p. P10005, 2018.

[122] A. M. Sirunyan *et al.*, "Search for physics beyond the standard model in high-mass diphoton events from proton-proton collisions at $\sqrt{s} = 13$ TeV," *Phys. Rev.*, vol. D98, no. 9, p. 092001, 2018.

[123] A. M. Sirunyan *et al.*, "Charged-particle nuclear modification factors in XeXe collisions at $\sqrt{s_{\mathrm{NN}}} = 5.44$ TeV," *JHEP*, vol. 10, p. 138, 2018.

[124] A. M. Sirunyan *et al.*, "Observation of Higgs boson decay to bottom quarks," *Phys. Rev. Lett.*, vol. 121, no. 12, p. 121801, 2018.

[125] A. M. Sirunyan *et al.*, "Measurement of jet substructure observables in $\mathrm{t\bar{t}}$ events from proton-proton collisions at $\sqrt{s} = 13$TeV," *Phys. Rev.*, vol. D98, no. 9, p. 092014, 2018.

[126] A. M. Sirunyan *et al.*, "Search for a charged Higgs boson decaying to charm and bottom quarks in proton-proton collisions at $\sqrt{s} = 8$ TeV," *JHEP*, vol. 11, p. 115, 2018.

[127] A. M. Sirunyan *et al.*, "Search for pair production of second-generation leptoquarks at $\sqrt{s} = 13$ TeV," *Phys. Rev.*, vol. D99, no. 3, p. 032014, 2019.

[128] A. M. Sirunyan *et al.*, "Search for an $L_\mu - L_\tau$ gauge boson using $\mathrm{Z} \to 4\mu$ events in proton-proton collisions at $\sqrt{s} = 13$ TeV," *Phys. Lett.*, vol. B792, pp. 345–368, 2019.

[129] A. M. Sirunyan *et al.*, "Search for long-lived particles with displaced vertices in multijet events in proton-proton collisions at $\sqrt{s} = 13$ TeV," *Phys. Rev.*, vol. D98, no. 9, p. 092011, 2018.

[130] A. M. Sirunyan *et al.*, "Search for pair-produced resonances decaying to quark pairs in proton-proton collisions at $\sqrt{s} = 13$ TeV," *Phys. Rev.*, vol. D98, no. 11, p. 112014, 2018.

[131] A. M. Sirunyan *et al.*, "Evidence for the associated production of a single top quark and a photon in proton-proton collisions at $\sqrt{s} = 13$ TeV," *Phys. Rev. Lett.*, vol. 121, no. 22, p. 221802, 2018.

[132] A. M. Sirunyan *et al.*, "Search for resonances in the mass spectrum of muon pairs produced in association with b quark jets in proton-proton collisions at $\sqrt{s} = 8$ and 13 TeV," *JHEP*, vol. 11, p. 161, 2018.

[133] A. M. Sirunyan *et al.*, "Search for production of Higgs boson pairs in the four b quark final state using large-area jets in proton-proton collisions at $\sqrt{s} = 13$ TeV," *JHEP*, vol. 01, p. 040, 2019.

[134] A. M. Sirunyan *et al.*, "Search for heavy resonances decaying into two Higgs bosons or into a Higgs boson and a W or Z boson in proton-proton collisions at 13 TeV," *JHEP*, vol. 01, p. 051, 2019.

[135] A. M. Sirunyan *et al.*, "Search for narrow $\mathrm{H}\gamma$ resonances in proton-proton collisions at $\sqrt{s} = 13$ TeV," *Phys. Rev. Lett.*, vol. 122, no. 8, p. 081804, 2019.

[136] A. M. Sirunyan *et al.*, "Search for a W' boson decaying to a τ lepton and a neutrino in proton-proton collisions at $\sqrt{s} = 13$ TeV," *Phys. Lett.*, vol. B792, pp. 107–131, 2019.

[137] A. M. Sirunyan *et al.*, "Searches for pair production of charginos and top squarks in final states with two oppositely charged leptons in proton-proton collisions at $\sqrt{s} = 13$ TeV," *JHEP*, vol. 11, p. 079, 2018.

[138] A. M. Sirunyan *et al.*, "Search for dark matter particles produced in association with a top quark pair at $\sqrt{s} = 13$ TeV," *Phys. Rev. Lett.*, vol. 122, no. 1, p. 011803, 2019.

[139] A. M. Sirunyan *et al.*, "Search for the Higgs boson decaying to two muons in proton-proton collisions at $\sqrt{s} = 13$ TeV," *Phys. Rev. Lett.*, vol. 122, no. 2, p. 021801, 2019.

[140] A. M. Sirunyan *et al.*, "Measurements of the differential jet cross section as a function of the jet mass in dijet events from proton-proton collisions at $\sqrt{s} = 13$ TeV," *JHEP*, vol. 11, p. 113, 2018.

[141] A. M. Sirunyan *et al.*, "Measurement of inclusive and differential Higgs boson production cross sections in the diphoton decay channel in proton-proton collisions at $\sqrt{s} = 13$ TeV," *JHEP*, vol. 01, p. 183, 2019.

[142] A. M. Sirunyan *et al.*, "Precision measurement of the structure of the CMS inner tracking system using nuclear interactions," *JINST*, vol. 13, no. 10, p. P10034, 2018.

[143] A. M. Sirunyan *et al.*, "Search for heavy resonances decaying into a vector boson and a Higgs boson in final states with charged leptons, neutrinos and b quarks at $\sqrt{s} = 13$ TeV," *JHEP*, vol. 11, p. 172, 2018.

[144] A. M. Sirunyan *et al.*, "Study of the underlying event in top quark pair production in pp collisions at 13 TeV," *Eur. Phys. J.*, vol. C79, no. 2, p. 123, 2019.

[145] A. M. Sirunyan *et al.*, "Search for supersymmetry in events with a τ lepton pair and missing transverse momentum in proton-proton collisions at $\sqrt{s} = 13$ TeV," *JHEP*, vol. 11, p. 151, 2018.

[146] A. M. Sirunyan *et al.*, "Measurement of differential cross sections for inclusive isolated-photon and photon+jets production in proton-proton collisions at $\sqrt{s} = 13$ TeV," *Eur. Phys. J.*, vol. C79, no. 1, p. 20, 2019.

[147] A. M. Sirunyan *et al.*, "Measurement of charged particle spectra in minimum-bias events from protonproton collisions at $\sqrt{s} = 13\,\text{TeV}$," *Eur. Phys. J.*, vol. C78, no. 9, p. 697, 2018.

[148] A. M. Sirunyan *et al.*, "Measurement of differential cross sections for Z boson pair production in association with jets at $\sqrt{s} = 8$ and 13 TeV," *Phys. Lett.*, vol. B789, pp. 19–44, 2019.

[149] A. M. Sirunyan *et al.*, "Search for heavy Majorana neutrinos in same-sign dilepton channels in proton-proton collisions at $\sqrt{s} = 13$ TeV," *JHEP*, vol. 01, p. 122, 2019.

[150] A. M. Sirunyan *et al.*, "Search for the decay of a Higgs boson in the $\ell\ell\gamma$ channel in proton-proton collisions at $\sqrt{s} = 13$ TeV," *JHEP*, vol. 11, p. 152, 2018.

[151] A. M. Sirunyan *et al.*, "Search for supersymmetric partners of electrons and muons in proton-proton collisions at $\sqrt{s} = 13$ TeV," *Phys. Lett.*, vol. B790, pp. 140–166, 2019.

[152] A. M. Sirunyan *et al.*, "Measurements of properties of the Higgs boson decaying to a W boson pair in pp collisions at $\sqrt{s} = 13$ TeV," *Phys. Lett.*, vol. B791, p. 96, 2019.

[153] A. M. Sirunyan *et al.*, "Search for dark matter produced in association with a Higgs boson decaying to $\gamma\gamma$ or $\tau^+\tau^-$ at $\sqrt{s} = 13$ TeV," *JHEP*, vol. 09, p. 046, 2018.

[154] A. M. Sirunyan *et al.*, "Observation of the Z$\to \psi\ell^+\ell^-$ decay in pp collisions at $\sqrt{s} =$ 13 TeV," *Phys. Rev. Lett.*, vol. 121, no. 14, p. 141801, 2018.

[155] A. M. Sirunyan *et al.*, "Search for resonant pair production of Higgs bosons decaying to bottom quark-antiquark pairs in proton-proton collisions at 13 TeV," *JHEP*, vol. 08, p. 152, 2018.

[156] A. M. Sirunyan *et al.*, "Search for a singly produced third-generation scalar leptoquark decaying to a τ lepton and a bottom quark in proton-proton collisions at $\sqrt{s} = 13$ TeV," *JHEP*, vol. 07, p. 115, 2018.

[157] A. M. Sirunyan *et al.*, "Search for pair-produced resonances each decaying into at least four quarks in proton-proton collisions at $\sqrt{s} = 13$ TeV," *Phys. Rev. Lett.*, vol. 121, no. 14, p. 141802, 2018.

[158] A. M. Sirunyan *et al.*, "Measurement of the weak mixing angle using the forward-backward asymmetry of Drell-Yan events in pp collisions at 8 TeV," *Eur. Phys. J.*, vol. C78, no. 9, p. 701, 2018.

[159] A. M. Sirunyan *et al.*, "Search for narrow and broad dijet resonances in proton-proton collisions at $\sqrt{s} = 13$ TeV and constraints on dark matter mediators and other new particles," *JHEP*, vol. 08, p. 130, 2018.

[160] A. M. Sirunyan *et al.*, "Angular analysis of the decay $\text{B}^+\to \text{K}^+\mu^+\mu^-$ in proton-proton collisions at $\sqrt{s} = 8$ TeV," *Phys. Rev.*, vol. D98, no. 11, p. 112011, 2018.

[161] A. M. Sirunyan *et al.*, "Search for beyond the standard model Higgs bosons decaying into a $\mathrm{b\bar{b}}$ pair in pp collisions at $\sqrt{s} = 13$ TeV," *JHEP*, vol. 08, p. 113, 2018.

[162] A. M. Sirunyan *et al.*, "Observation of the $\chi_{\mathrm{b1}}(3\mathrm{P})$ and $\chi_{\mathrm{b2}}(3\mathrm{P})$ and measurement of their masses," *Phys. Rev. Lett.*, vol. 121, p. 092002, 2018.

[163] A. M. Sirunyan *et al.*, "Constraints on models of scalar and vector leptoquarks decaying to a quark and a neutrino at $\sqrt{s} = 13$ TeV," *Phys. Rev.*, vol. D98, no. 3, p. 032005, 2018.

[164] A. M. Sirunyan *et al.*, "Search for an exotic decay of the Higgs boson to a pair of light pseudoscalars in the final state with two b quarks and two τ leptons in proton-proton collisions at $\sqrt{s} = 13$ TeV," *Phys. Lett.*, vol. B785, p. 462, 2018.

[165] A. M. Sirunyan *et al.*, "Measurement of the production cross section for single top quarks in association with W bosons in proton-proton collisions at $\sqrt{s} = 13$ TeV," *JHEP*, vol. 10, p. 117, 2018.

[166] A. M. Sirunyan *et al.*, "Search for black holes and sphalerons in high-multiplicity final states in proton-proton collisions at $\sqrt{s} = 13$ TeV," *JHEP*, vol. 11, p. 042, 2018.

[167] A. M. Sirunyan *et al.*, "Search for top squarks decaying via four-body or chargino-mediated modes in single-lepton final states in proton-proton collisions at $\sqrt{s} = 13$ TeV," *JHEP*, vol. 09, p. 065, 2018.

[168] A. M. Sirunyan *et al.*, "Measurement of the groomed jet mass in PbPb and pp collisions at $\sqrt{s_{\mathrm{NN}}} = 5.02$ TeV," *JHEP*, vol. 10, p. 161, 2018.

[169] A. M. Sirunyan *et al.*, "Search for an exotic decay of the Higgs boson to a pair of light pseudoscalars in the final state of two muons and two τ leptons in proton-proton collisions at $\sqrt{s} = 13$ TeV," *JHEP*, vol. 11, p. 018, 2018.

[170] A. M. Sirunyan *et al.*, "Search for vector-like T and B quark pairs in final states with leptons at $\sqrt{s} = 13$ TeV," *JHEP*, vol. 08, p. 177, 2018.

[171] A. M. Sirunyan *et al.*, "Constraining gluon distributions in nuclei using dijets in proton-proton and proton-lead collisions at $\sqrt{s_{\mathrm{NN}}} = 5.02$ TeV," *Phys. Rev. Lett.*, vol. 121, no. 6, p. 062002, 2018.

[172] A. M. Sirunyan *et al.*, "Measurement of prompt $\psi(2\mathrm{S})$ production cross sections in proton-lead and proton-proton collisions at $\sqrt{s_{\mathrm{NN}}} = 5.02$ TeV," *Phys. Lett.*, vol. B790, pp. 509–532, 2019.

[173] A. M. Sirunyan *et al.*, "Measurement of the top quark mass with lepton+jets final states using p p collisions at $\sqrt{s} = 13\,\mathrm{TeV}$," *Eur. Phys. J.*, vol. C78, no. 11, p. 891, 2018.

[174] A. M. Sirunyan *et al.*, "Elliptic flow of charm and strange hadrons in high-multiplicity pPb collisions at $\sqrt{s_{\mathrm{NN}}} = 8.16$ TeV," *Phys. Rev. Lett.*, vol. 121, no. 8, p. 082301, 2018.

[175] A. M. Sirunyan *et al.*, "Search for disappearing tracks as a signature of new long-lived particles in proton-proton collisions at $\sqrt{s} = 13$ TeV," *JHEP*, vol. 08, p. 016, 2018.

[176] A. M. Sirunyan *et al.*, "Measurement of differential cross sections for Z boson production in association with jets in proton-proton collisions at $\sqrt{s} = 13$ TeV," *Eur. Phys. J.*, vol. C78, no. 11, p. 965, 2018.

[177] A. M. Sirunyan *et al.*, "Search for $\mathrm{t\bar{t}H}$ production in the $\mathrm{H} \to \mathrm{b\bar{b}}$ decay channel with leptonic $\mathrm{t\bar{t}}$ decays in proton-proton collisions at $\sqrt{s} = 13$ TeV," *JHEP*, vol. 03, p. 026, 2019.

[178] A. M. Sirunyan *et al.*, "Measurements of Higgs boson properties in the diphoton decay channel in proton-proton collisions at $\sqrt{s} = 13$ TeV," *JHEP*, vol. 11, p. 185, 2018.

[179] A. M. Sirunyan *et al.*, "Observation of $t\bar{t}H$ production," *Phys. Rev. Lett.*, vol. 120, no. 23, p. 231801, 2018.

[180] A. M. Sirunyan *et al.*, "Search for a new scalar resonance decaying to a pair of Z bosons in proton-proton collisions at $\sqrt{s} = 13$ TeV," *JHEP*, vol. 06, p. 127, 2018. [Erratum: JHEP03,128(2019)].

[181] A. M. Sirunyan *et al.*, "Search for high-mass resonances in final states with a lepton and missing transverse momentum at $\sqrt{s} = 13$ TeV," *JHEP*, vol. 06, p. 128, 2018.

[182] A. M. Sirunyan *et al.*, "Search for a heavy right-handed W boson and a heavy neutrino in events with two same-flavor leptons and two jets at $\sqrt{s} = 13$ TeV," *JHEP*, vol. 05, no. 05, p. 148, 2018.

[183] A. M. Sirunyan *et al.*, "Search for a heavy resonance decaying into a Z boson and a Z or W boson in 22q final states at $\sqrt{s} = 13$ TeV," *JHEP*, vol. 09, p. 101, 2018.

[184] A. M. Sirunyan *et al.*, "Measurement of differential cross sections for the production of top quark pairs and of additional jets in lepton+jets events from pp collisions at $\sqrt{s} = 13$ TeV," *Phys. Rev.*, vol. D97, no. 11, p. 112003, 2018.

[185] A. M. Sirunyan *et al.*, "Search for new physics in dijet angular distributions using protonproton collisions at $\sqrt{s} = 13$ TeV and constraints on dark matter and other models," *Eur. Phys. J.*, vol. C78, no. 9, p. 789, 2018.

[186] A. M. Sirunyan *et al.*, "Search for $t\bar{t}H$ production in the all-jet final state in proton-proton collisions at $\sqrt{s} = 13$ TeV," *JHEP*, vol. 06, p. 101, 2018.

[187] A. M. Sirunyan *et al.*, "Search for additional neutral MSSM Higgs bosons in the $\tau\tau$ final state in proton-proton collisions at $\sqrt{s} = 13$ TeV," *JHEP*, vol. 09, p. 007, 2018.

[188] A. M. Sirunyan *et al.*, "Search for high-mass resonances in dilepton final states in proton-proton collisions at $\sqrt{s} = 13$ TeV," *JHEP*, vol. 06, p. 120, 2018.

[189] A. M. Sirunyan *et al.*, "Evidence for associated production of a Higgs boson with a top quark pair in final states with electrons, muons, and hadronically decaying τ leptons at $\sqrt{s} = 13$ TeV," *JHEP*, vol. 08, p. 066, 2018.

[190] A. M. Sirunyan *et al.*, "Observation of proton-tagged, central (semi)exclusive production of high-mass lepton pairs in pp collisions at 13 TeV with the CMS-TOTEM precision proton spectrometer," *JHEP*, vol. 07, p. 153, 2018.

[191] A. M. Sirunyan *et al.*, "Jet properties in PbPb and pp collisions at $\sqrt{s_{\mathrm{N\,N}}} = 5.02$ TeV," *JHEP*, vol. 05, p. 006, 2018.

[192] A. M. Sirunyan *et al.*, "Search for a heavy resonance decaying to a pair of vector bosons in the lepton plus merged jet final state at $\sqrt{s} = 13$ TeV," *JHEP*, vol. 05, p. 088, 2018.

[193] A. M. Sirunyan *et al.*, "Search for narrow resonances in the b-tagged dijet mass spectrum in proton-proton collisions at $\sqrt{s} = 8$ TeV," *Phys. Rev. Lett.*, vol. 120, no. 20, p. 201801, 2018.

[194] A. M. Sirunyan *et al.*, "Search for natural and split supersymmetry in proton-proton collisions at $\sqrt{s} = 13$ TeV in final states with jets and missing transverse momentum," *JHEP*, vol. 05, p. 025, 2018.

[195] A. M. Sirunyan *et al.*, "Search for lepton-flavor violating decays of heavy resonances and quantum black holes to e final states in proton-proton collisions at $\sqrt{s} = 13$ TeV," *JHEP*, vol. 04, p. 073, 2018.

[196] A. M. Sirunyan *et al.*, "Comparing transverse momentum balance of b jet pairs in pp and PbPb collisions at $\sqrt{s_{\mathrm{NN}}} = 5.02$ TeV," *JHEP*, vol. 03, p. 181, 2018.